To the Graduate Council:

I am submitting herewith a thesis written by Michael J. Haass entitled "Design and Performance of a Varied Line Space Grating Soft X-ray Monochromator." I have examined the final copy of this thesis for form and content and recommend that it be accepted in partial fulfillment of the requirements for the degree of Master of Science, with a major in Physics.

Thomas A. Callcott

Thomas A. Callcott, Major Professor

We have read this thesis
and recommend its acceptance:

Marianne Breinig

David J. Pegg

Accepted for the Council:

C W Minkel

Associate Vice Chancellor
and Dean of the Graduate School

STATEMENT OF PERMISSION TO USE

In presenting this thesis in partial fulfillment of the requirements for a Master's of Science degree at The University of Tennessee, Knoxville, I agree that the Library shall make it available to borrowers under rules of the Library. Brief quotations from this thesis are allowable without special permission, provided that accurate acknowledgment of the source is made.

Permission for extensive quotation from or reproduction of this thesis may be granted by my major professor, or in his absence, by the Head of Interlibrary Services when, in the opinion of either, the proposed use of the material is for scholarly purposes. Any copying or use of the material in this thesis for financial gain shall not be allowed without my written permission.

Signature Michael J. Haase

Date 7-12-93

DESIGN AND PERFORMANCE OF A VARIED LINE SPACE GRATING SOFT X-RAY MONOCHROMATOR

A Thesis

Presented for the

Master of Science

Degree

The University of Tennessee, Knoxville

Michael J. Haass

August 1993

ACKNOWLEDGEMENTS

The work contained in this thesis and all of the preparation leading up to its conclusion could not have been accomplished without the help many people who have touched my life in the past three years. I wish I could list each person's name and the help they provided, but time and space here are limited. Suffice it to say that if you are reading this, you are probably one of the people I should thank.

Significant help at The University of Tennessee has come from my major professor, T. A. Callcott. I would like to thank Dr. Callcott for letting me work on an optics project, even though his research group concentrates on condensed matter physics, and for all the conversations that lead to the completion of this work. Additional indispensable help at UT came from Dr. J. J. Jia. Thanks, JJ, for proofreading and all the coffee. I would also like to thank the other two members of my thesis committee, Dr. M. Breinig and Dr. D. Pegg for the time they committed and the contributions they made to my success in this undertaking.

Without help from many people at the National Institute of Standards and Technology, Gaithersburg, Maryland, I would probably still be at NIST tinkering with the "fine adjust." Richard Watts and Charles Tarrio both made significant contributions through their patience in answering all my questions. Luckily, they shared some of my interest in issues, basketball and home-brew, or the visits to NIST would have seemed much longer.

Finally, special thanks must go to my partner of the past seven years. Sonya's contributions to this document are immeasurable. Her proofreading skills and patience were tested throughout the past month, but her most significant contributions were made by reminding me of what is most important, thereby keeping me on an even keel to the finish.

ABSTRACT

This thesis discusses the design and performance of a varied line space (VLS) grating soft x-ray monochromator constructed at the Synchrotron Ultraviolet Radiation Facility (SURF II), at the National Institute of Standards and Technology (NIST), Gaithersburg, Maryland. Advantages of the design include fixed entrance and exit slits, fixed entrance and exit axes, simple optical elements, simple wavelength scanning, moderate resolving powers and good throughput. Topics addressed in detail are: focusing properties of VLS gratings, ray tracing studies of the NIST beamline, and the performance of the assembled monochromator. Ray tracing studies show that resolving powers in excess of 1000 and throughput of 8 x 10^9 photons/sec/mA should be attainable. Commissioning of the beamline at NIST has produced resolving powers on the order of 700 and throughput of 6 x 10^9 photons/sec/mA. Some background information on the characteristics of synchrotron radiation and standard soft x-ray monochromator designs will also be presented.

TABLE OF CONTENTS

SECTION	PAGE
1. INTRODUCTION	1
2. CHARACTERISTICS OF SYNCHROTRON RADIATION	4
3. DESIGN REQUIREMENTS	9
4. REVIEW OF STANDARD DESIGNS	11
5. FOCUSING PROPERTIES OF THE VARIED LINE SPACE GRATING	14
5.1 Depth of Focus	21
6. RAY TRACING STUDIES	29
6.1 Resolving Power	34
6.2 Losses and Throughput	46
6.3 Alignment errors	47
7. EXPERIMENTAL EVALUATION	49
7.1 Experimental Procedure	49
7.2 Results	50
8. SUMMARY	62
LIST OF REFERENCES	64
APPENDIX	67
VITA	68

LIST OF FIGURES

Figure		Page
1.	Spectral output of SURF II electron storage ring at 284 MeV.	5
2.	Degree of polarization of SURF II synchrotron light at 100 Å.	7
3.	Geometry for VLS grating focusing properties.	15
4.	Focal curve for high energy grating with constant line space density, $\sigma = a_0$.	22
5.	Focal curve for high energy grating with linear variation in the line space density, $\sigma = a_0 + a_1x$.	22
6.	Focal curve for high energy grating with linear and quadratic variation in the line space density, $\sigma = a_0 + a_1x + a_2x^2$.	23
7.	Focal curve for low energy grating with constant line space density, $\sigma = a_0$.	24
8.	Focal curve for low energy grating with linear variation in the line space density, $\sigma = a_0 + a_1x$.	24

9. Focal curve for low energy grating with linear and quadratic variation in the line space density, $\sigma = a_0 + a_1x + a_2x^2$. 25

10. Geometry for depth of focus calculation. 26

11. Depth of focus as a function of wavelength for high energy grating. 27

12. Depth of focus as a function of wavelength for low energy grating. 27

13. Schematic of NIST bl-7 monochromator showing relative positioning of optical elements and slits. 30

14. Schematic of NIST bl-7 monochromator showing relative positioning of optical elements and vacuum components. 30

15. Example of beam profile from SHADOW at source. 35

16. Example of beam profile from SHADOW; footprint on the condensing mirror. 35

17. Example of beam profile from SHADOW; image at entrance slit. 36

18. Example of beam profile from SHADOW; footprint on the collimating mirror. 36

19. Example of beam profile from SHADOW;
footprint on high energy grating. 37

20. Example of beam profile from SHADOW;
image from high energy grating. 37

21. Example of beam profile from SHADOW;
footprint on low energy grating. 38

22. Example of beam profile from SHADOW;
image from low energy grating. 38

23. NIST bl-7 monochromator ray trace output at 400Å,
0.01 cm exit slit width, showing Gaussian distribution
of wavelength through exit slit. 39

24. Predicted resolving power of NIST bl-7 monochromator
as a function of wavelength. 41

25. Predicted resolving power of NIST bl-7 monochromator,
with high energy grating, as a function of exit slit width. 42

26. Predicted resolving power of NIST bl-7 monochromator,
at 100Å and 0.025 cm exit slit width, as a function
of entrance slit width. 44

27. Image of 0.05 cm entrance slit formed by condensing
mirror and collimating mirror. 45

28. Image of 0.01 cm entrance slit formed by condensing mirror and collimating mirror. 45

29. Effect of angle of incidence on grating focal distance. 48

30. Aluminum absorption edge using low energy grating. 51

31. Beryllium absorption edge using high energy grating. 51

32. Carbon absorption edge using high energy grating. 53

33. Silicon absorption edge using low energy grating. 54

34. Silicon absorption edge using high energy grating. 55

35. Measured resolving power of NIST bl-7 monochromator, shown as a function of wavelength. 56

36. Measured resolving power of NIST bl-7 monochromator, shown as a function of exit slit width. 57

37. Silicon absorption edge recorded using electron energy loss spectroscopy. 59

1. INTRODUCTION

Synchrotron radiation was first used as a research tool by Tomboulian and Hartman, [1] at the 300 MeV Cornell Synchrotron in 1956, for far-ultraviolet and soft x-ray absorption spectroscopy studies of metallic beryllium and aluminum. Previous work by theorists [2-5] in the late 1940's and early 1950's predicted the unique characteristics of synchrotron radiation; in particular, the broad band continuous spectrum extending from the infrared to a cut off in the x-ray region that depends on the energy and bending radius of the stored electrons. Synchrotron radiation was first observed and characterized at the General Electric Laboratories in Schenectady, New York in 1946 [6]. Strictly speaking, a synchrotron is an accelerator, but the term synchrotron is commonly used to describe storage rings. Shown to be an excellent research tool, many synchrotron facilities have been constructed in the United States and overseas. Synchrotron radiation is currently used in a broad variety of research disciplines such as physics, biology and chemistry. In condensed matter physics, synchrotron radiation has become a very important tool providing a stable source of radiation in a practical and previously unexplored energy range. Today, synchrotron radiation provides the means to study the effects of valence and core electron states on the optical properties of solids.

An essential element of any experiment using synchrotron radiation is a dispersion device that allows the user to select a portion of the broad band radiation spectrum. For hard x-rays, dispersion is provided by Bragg diffraction from a crystal, while for soft x-rays a ruled grating can be used. This work characterizes a soft x-ray monochromator design that effectively meets the unique design challenges of beamline monochromators for synchrotron light sources. While in no way comprehensive, a brief summary of some standard designs will help to introduce the basic criteria needed to compare the performance of different monochromators and to illustrate the current technologies in the field.

A recent development in x-ray monochromator design is the use of a planar, varied line space (VLS) grating as the dispersing element. The VLS grating based designs have many attractive features when compared with conventional designs. The most important features are simplified optical elements and a relatively constant focal plane over a range of wavelengths.

Before settling on the particulars of a design, one would like to be able to predict the performance of the instrument. Analytical predictions are made exceedingly complicated by unconventional electron beam light sources and aberrations from grazing incidence optics. The simplest way to overcome these difficulties is to use a computer to trace light rays through the optical system. While some commercial ray tracing programs are available for personal computers, evaluating relatively complex systems consisting of a synchrotron source and monochromator is impractical because of long waits for calculation results and the difficulties involved in modeling bending magnet radiation as well as off axis, aspheric optics. A very useful and increasingly popular ray tracing package, SHADOW, has been developed under the direction of F. Cerrina at the University of Wisconsin, Madison. SHADOW is optimized for use in studying optical systems with synchrotron sources and is available as public domain software for use on mainframe computers.

The goal of this work is to present a thorough analysis of a soft x-ray monochromator built on a design pronciple presented in a previous paper [7] and compare the actual performance to the predicted performance. In the original design, an analytical method was used to derive the variation in the line space density of a plane grating in order to provide a relatively fixed focal distance over a range of wavelengths. A computer ray tracing package has been used to calculate the resolving power and throughput of the instrument design. After construction, the performance of the monochromator was evaluated and the resolving power and throughput were measured and compared to the predicted performance.

2. CHARACTERISTICS OF SYNCHROTRON RADIATION

For the purpose of monochromator design, the electron storage ring can be treated as a black box. The detailed analysis of radiation emitted by accelerating charged particles, and synchrotron radiation in particular, is presented in the literature [5]. As a brief overview of the characteristics of synchrotron radiation, significant results will be quoted. An in depth summary of synchrotron radiation can be found in chapter two of G. Margaritondo's book, Introduction to Synchrotron Radiation [8]. This discussion will be confined to radiation from bending magnets.

The power radiated by an electron moving in a circular orbit increases as the fourth power of the electron's energy and is given by:

$$P = \frac{2e^2cE^4}{3\rho^2(m_oc^2)^4} \qquad \text{(cgs units)} \qquad (1)$$

where ρ is the radius of the orbit. The spectral distribution of the radiation as a function of wavelength is given by:

$$\frac{dI}{d\omega} = 2\sqrt{3}\frac{e^2}{c}\gamma\frac{\omega}{\omega_c}\int_{2\omega/\omega_c}^{\infty} K_{5/3}(x)dx \qquad \text{(cgs units)} \qquad (2)$$

where $\gamma = E/m_oc^2$, ω is the angular frequency, and $K_{5/3}$ is a modified Bessel function of the second kind. The spectral distribution of SURF II is shown in figure 1. The quantity $\lambda_c = 2\pi c/\omega_c$ is called the critical photon wavelength and is given by $\lambda_c = 4\pi\rho/3\gamma^3$. The critical wavelength is useful for comparing the spectral output of different synchrotron sources. Half of the radiated power is emitted at wavelengths above λ_c and half below λ_c. However, the available light intensity from a source falls off rapidly at wavelengths smaller than λ_c. A

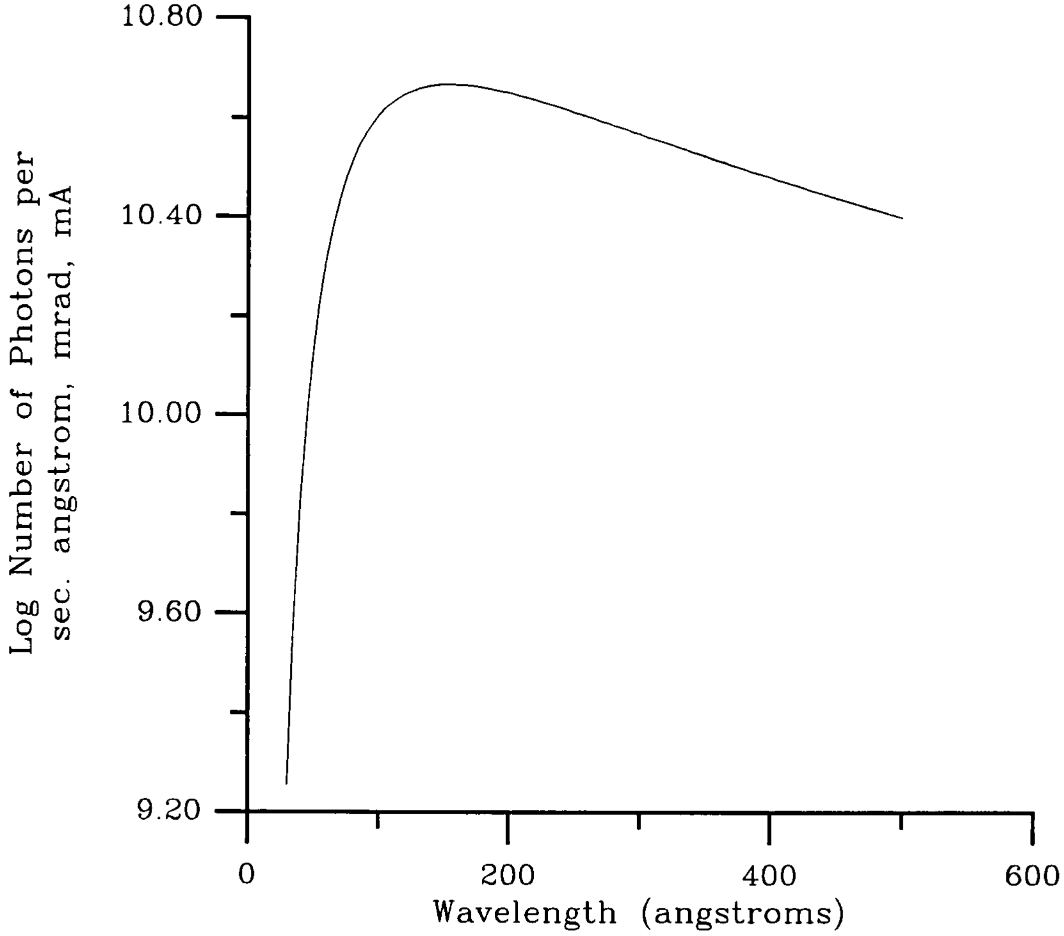

Figure 1. Spectral output of SURF II electron storage ring at 284 MeV.

second parameter that is useful in comparing synchrotron sources is the spectral brightness. Brightness is defined as the number of photons emitted in a 0.1% bandwidth centered at a photon energy, $h\nu$, per unit time, dt, ring current, i, solid angle, $d\Omega$, and source area, $dxdy$:

$$b = \frac{dn(x,z,\theta,\psi,h\nu)}{idxdyd\Omega dt}.$$

Since the brightness is a function of many variables, it is sometimes easier to define another parameter, the central brightness. This is the brightness of the source in the plane of the electron orbit and tangent to the orbit at the reference point, $x = z = 0$. This definition makes the central brightness a function of photon energy only, thus avoiding the details of a particular user's beamline geometry.

For some experiments, it is necessary to know something about the polarization of the light from the storage ring. For light polarized with the electric vector parallel to the plane of the electron orbit, the emitted power is proportional to $K^2_{2/3}(\xi)$. For light polarized with the electric vector perpendicular to the plane of the electron orbit, the emitted power is proportional to $(\psi\gamma)^2 K^2_{1/3}(\xi)/[1+(\psi\gamma)^2]$. The normalized intensity of the two components is shown in the figure 2. The important features are that only parallel polarized light is found in the orbital plane, and above and below the orbital plane the light is eliptically polarized. The vertical angular spread of the parallel polarized light is on the order of $1/\gamma$. The two components of polarized light combine to give the light a gaussian distribution in the planes parallel and perpendicular to the orbital plane. The quantities σ_x and σ_z are used to denote the half widths of the beam in the parallel and perpendicular planes respectively.

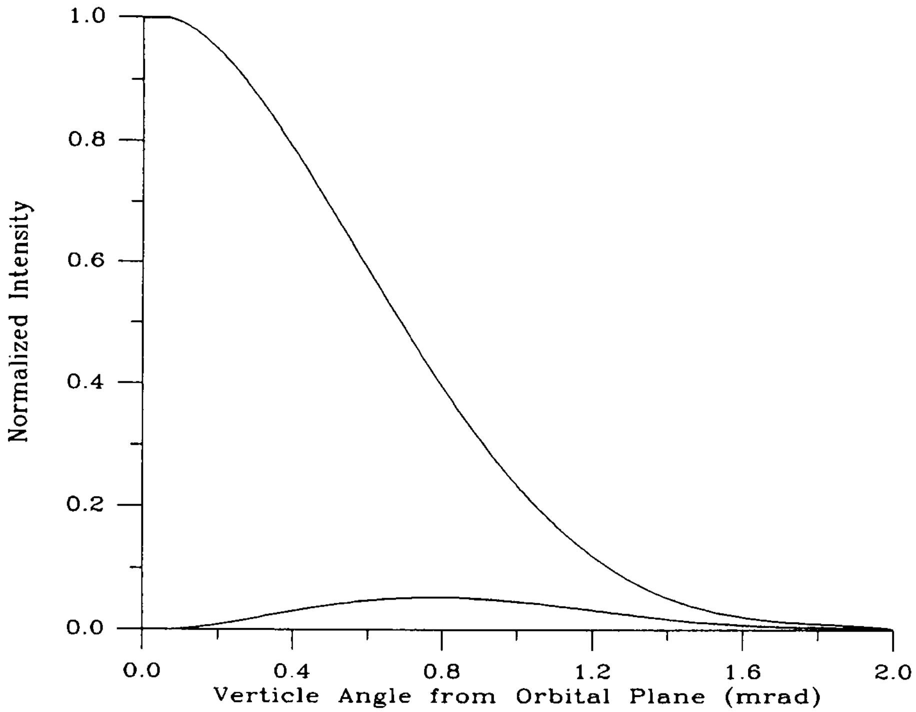

Figure 2. Degree of Polarization of SURF II synchrotron light at 100 Å. Upper curve shows normalized intensity of parallel polarized light, lower curve shows normalized intensity of perpendicular polarized light.

Since the electrons orbit at nearly the speed of light, the time structure of the source is easily deduced from a knowledge of the radius of the electron orbit and the electron bunch length. For the SURF II storage ring, ρ = 83.82 cm and the bunch length is approximately 1.5 nanoseconds. At any given time there are two electron bunches orbiting in the ring, so that a light pulse of 1.5 nanoseconds in duration will be observed every 8.5 nanoseconds. Table 1 summarizes the specifics of the SURF II storage ring.

Table 1. SURF II Electron Storage Ring Parameters.

Ring Characteristic	SURF II Value
Weak focusing, single magnet	
Straight sections	None
Radius of electron orbit	83.8212 cm
σ_x	0.085 (2 mm)
σ_y	0.042 (1 mm)
Divergence	$\pm$10 mrad horizontal $\pm$1.5 mrad vertical
Energy	284 MeV normal operating 10 - 300 MeV accessible
Record beam current	326 mA
Normal operating current	$\approx$300 mA
Number of electron bunches	2, 1.5 nanoseconds in length

3. DESIGN REQUIREMENTS

The characteristics of a synchrotron source impose certain requirements on the design of a monochromator. The NIST beamline seven (bl-7) monochromator is intended for use in the soft x-ray region where all materials are opaque. Therefore no windows may be used to isolate sections of the instrument from the synchrotron ring. This requires that the entire beamline be operated under ultra-high vacuum (UHV) conditions in order to maintain the vacuum requirements of the storage ring. Fast action pneumatic valves must be incorporated in the design to isolate the beamline in the event of a loss of vacuum in the user's instrument. Since materials are opaque to soft x-rays, only reflective optics may be employed in the design. Because of the low reflectivity of the optical elements in this region, grazing angles of incidence ($\alpha \geq 80^{\circ}$) must be used and the number of reflecting surfaces should be minimized. Due to large aberrations from grazing incidence optics, the imaging quality of various surface figures should be considered.

Spherical mirrors introduce astigmatism, coma and spherical aberrations. An astigmatic image of a point source will exhibit two focal points located at different points along the optical axis. At one point, the meridial focal point, the point source will be imaged as a line in the plane of the mirror surface. At the sagittal focal point, the source will be imaged as a line in the plane perpendicular to the mirror surface. For a spherical mirror, the ratio of the meridial focal length to the sagittal focal length is equal to the square of the sine of the grazing angle of incidence, $f_m/f_s = \sin^2\theta_i$. At normal incidence, $\theta_i = 90$ degrees, the ratio f_m/f_s is equal to one and the two focal points coincide. However, at $\theta_i = 3$ degrees, f_m/f_s is about 0.003 and the sagittal focal length is about 350 times the meridial focal length. Coma arises at grazing angles of incidence because different parts of the mirror are at different distances from the source. This causes the magnification to vary along the surface of the mirror. Spherical aberration introduces a variation in the image distance with position on the mirror surface. Coma and spherical aberration can be reduced by using smaller mirrors or apertures, but at the expense of image brightness. Toroidal mirrors reduce astigmatism but not spherical aberration, while elliptical mirrors reduce spherical aberration but not astigmatism. A single mirror can not eliminate coma. Another method of reducing aberrations employs multiple mirrors, but this, again, reduces image brightness [9].

Other design influences are the desirability of high throughput, fixed entrance and exit axes, fixed entrance and exit slits and suppression of higher order reflections from the gratings. Additional attention should be paid to the physical space limitations and geometry of the synchrotron facility. For example, the NIST (bl-7) passes through a six-foot thick cement radiation shielding wall.

4. REVIEW OF STANDARD DESIGNS

The performance of a monochromator is usually judged by two factors: the resolving power and the photon flux. Resolving power is defined as the ratio of desired wavelength (energy) to the spread in wavelength (energy) delivered, $\lambda/\Delta\lambda$, ($E/\Delta E$). Sometimes only the resolution, $\Delta\lambda$ (ΔE) is reported. Theoretically, the resolving power of an instrument is set by the grating, but in practice it is usually aberrations or surface figure errors in the other focusing elements that limit performance. An entrance slit is often used to increase resolving power by effectively decreasing the size of the source in the diffraction plane. An exit slit is necessary to select the desired wavelength. Smaller entrance and exit slits increase resolving power, but at the expense of photon flux (throughput). Other factors that affect the instrument throughput are geometrical losses in the optical system (light rays missing an element) and the reflectivity of the optical surfaces. Some users are also interested in the type and degree of polarization the monochromator provides. This, too, can be affected by the reflectivity of the optical surfaces as well as by the position, relative to the orbital plane, from which the light is collected.

Monochromator designs are generally characterized by the surface figure of their dispersing element. Common designs for the soft x-ray region employ toroidal, spherical, cylindrical or plane gratings at grazing angles of incidence. A plethora of instruments are in use and are characterized in the literature [10]. The following is a summary of some standard designs.

The simple Rowland-circle instrument is perhaps the most elementary design. It is based on the focusing properties of a spherical grating. The grating will focus the diffracted light on a circle of diameter equal to the radius of curvature of the grating with the center of the grating lying on the Rowland circle. The apparent simplicity of this design, a single focusing element providing high throughput and good resolution, is an attractive feature. However, at grazing incidence, the spherical surface figure introduces a large astigmatism that can only be overcome by the addition of pre-focusing optics thereby reducing throughput. Additional disadvantages of this design are the lack of a fixed exit axis and exit slit position.

The desire for a fixed exit axis and exit slit position combined with the good resolving power of a Rowland circle instrument is satisfied by the "grasshopper" design. This design employs a combination of translations and rotations of a pre-focusing mirror, mirror - slit assembly, and grating to provide the fixed exit axis and slit position. As the monochromator scans, a pre-focusing mirror translates along the beam axis at a fixed angle of incidence while the grating moves along the Rowland circle. Rotation and translation of the mirror - slit assembly redirects the light from the pre-focusing mirror to the grating. The grasshopper design has produced resolving powers in excess of 1000 [11]. The chief disadvantage of this design is the complicated and precision motion required for wavelength scanning.

The aberration effects in the simple Rowland-circle monochromator are avoided in the toroidal grating monochromator (TGM). This improves throughput by reducing the number of astigmatic pre-focusing elements and provides a fixed exit axis. Disadvantages of this design are that focal distance is a strong function of wavelength, and toroidal surface figures are difficult to manufacture and rule. The resolution can be improved by designing a movable exit slit that follows the focal point as the wavelength is scanned, but this requires that any subsequent experiment chamber also move with wavelength scanning. Even with a movable exit slit, the instrument resolving power is often limited by inaccuracies in the surface figure of the grating. A number of toroidal grating monochromators are in use with reported resolving powers on the order of 1000 [12-14].

Improving on the TGM design, Chen [15-16] has presented the design of a cylindrical element monochromator (CEM - later called the "dragon"). In this design two cylindrical pre-focusing mirrors are used to de-couple the focusing in the vertical and horizontal directions and a cylindrical grating provides dispersion. Since cylindrical elements are easier to manufacture than toroidal elements, surface figure errors are small and do not limit the resolving power of the instrument. The focal distance is still a strong function of wavelength, so this design also incorporates a movable exit slit. Resolving powers of 3000 to 5000 are predicted.

All aberrations from the grating, and nearly all surface figure errors are eliminated in the plane grating design. Pre-focusing mirrors must be used to collimate the beam onto the grating and a post-focusing mirror used to re-focus the light on the exit slit. A plane grating monochromator (dubbed the SX-700) that uses an elliptical pre-focusing mirror and a fixed, curved exit slit has produced resolving powers on the order of 10000 [17]. Wavelength scanning is accomplished by rotations of the plane mirror and grating while the fixed exit slit position is maintained by a movable plane mirror before the grating and by movement of the grating itself.

5. FOCUSING PROPERTIES OF THE VARIED LINE SPACE GRATING

A constant line space, plane grating at grazing incidence in a converging beam of light has a focal distance, r(λ), that varies strongly with wavelength. One way to accommodate a monochromater design to this varying focal distance is to allow the exit slit to be moved to the correct position as the wavelength is scanned (another is forego the plane grating altogether and employ a concave grating). The first method of accommodation is inconvenient in that any experiment chamber after the monochromater must then also move with the exit slit. This can become impractical if the experiment chamber is large or very heavy. The second method of accommodation requires an optical element that is difficult to fabricate, thus resulting in elements with significant surface figure or slope errors that degrade their imaging quality. These focusing gratings also introduce large aberrations when used at grazing incidence.

The chief cause of the variation in focal distance is that the grazing angle of incidence for a non-collimated beam varies along the optical axis of the grating, thus causing variations in the angle of diffraction as dictated by the grating equation, $n\lambda = d(\sin\alpha - \sin\beta)$. It has been noted by Callcott *et. al.* and others [7,18-21] that a variation in the line density as a function of position on the grating surface could reduce or eliminate the problem. The following discussion will closely follow the work of Callcott *et. al*[7]. Using simple geometry and the grating equation, the linear and quadratic terms in the line space density, $\sigma = a_0 + a_1 x + a_2 x^2$, will be derived.

The plane grating is placed in a beam of converging light that forms a virtual object at a distance, r_0, from the grating center (the particular geometry is shown in figure 3). The simple focusing condition will be that rays diffracted

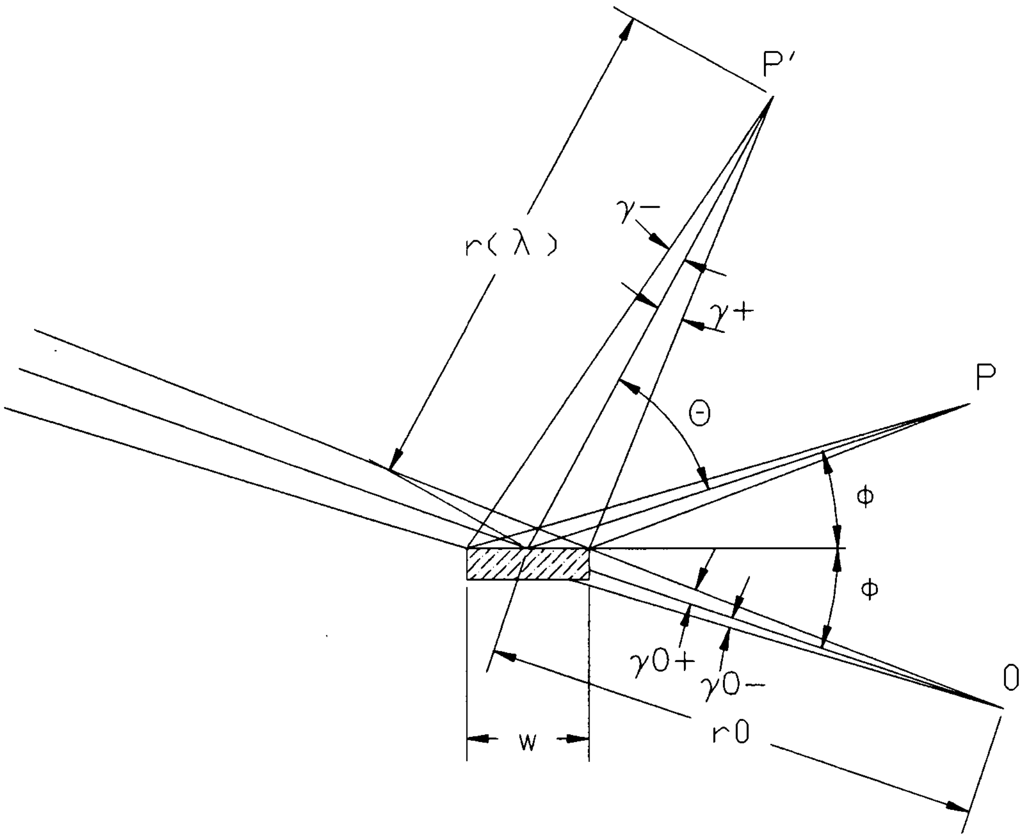

Figure 3. Geometry for VLS grating focusing properties. w = 0 at center of grating and positive on image side of grating center.

from either end of the grating intersect the diffracted central ray at the same point, P', a distance, r, from the grating center. The zero order light is reflected at an angle, ϕ, from the grating surface and is focused at a point P also a distance r_0, from the grating center. The diffracted light is displaced by an angle, θ, from the zero order reflected light and the angles, $\gamma^{\pm}$, between the central ray and the rays diffracted from either end of the grating at a position, w, from the grating center are set by the focusing condition. The diffraction condition for a ray at an arbitrary point on the grating surface is:

$$\frac{n\lambda}{d_0 + \delta(w)} = \cos(\phi + \gamma_0^{\pm}) - \cos(\phi + \theta + \gamma^{\pm}) \tag{3}$$

where d_0 is the line spacing at the grating center, n is the spectral order, and $\gamma_0^{\pm}$ are the angles between the zero order central ray and the rays reflected from either end of the grating. The diffraction condition for the ray striking the grating center, $w = 0$, is:

$$\frac{n\lambda}{d_0} = \cos\phi - \cos(\phi + \theta). \tag{4}$$

The angles $\gamma_0^{\pm}$ for rays reflected in zero order from the grating surface at positions w and -w are given by the law of sines:

$$\frac{\pm w}{\sin(\gamma_0^{\pm})} = \frac{r_0}{\sin(\phi + \gamma_0^{\pm})},$$

$$\sin(\gamma_0^{\pm}) = \frac{\pm w}{r_0}\sin(\phi + \gamma_0^{\pm}). \tag{5a}$$

The angles $\gamma^{\pm}$ for rays diffracted from the grating surface at positions w and -w are similarly given by:

$$\frac{\pm w}{\sin(\gamma^{\pm})} = \frac{r}{\sin(\phi + \theta + \gamma^{\pm})} \quad ,$$

$$\sin(\gamma^{\pm}) = \frac{\pm w}{r}\sin(\phi + \theta + \gamma^{\pm}). \tag{5b}$$

For simplicity, we look only at $x > 0$ and expand equations (3), (5a) and (5b) by trigonometric addition formulas to give:

$$\frac{n\lambda}{d_0 + \delta(x)} = \cos\phi\cos\gamma_0 - \sin\phi\sin\gamma_0 - \cos(\phi+\theta)\cos\gamma + \sin(\phi+\theta)\sin\gamma\,, \tag{6}$$

$$\sin\gamma_0 = \frac{w}{r_0}(\sin\phi\cos\gamma_0 + \cos\phi\sin\gamma_0), \tag{7a}$$

$$\sin\gamma = \frac{w}{r}\left[\sin(\phi+\theta)\cos\gamma + \cos(\phi+\theta)\sin\gamma\right]. \tag{7b}$$

Dividing through by $\sin\gamma_o$ and $\sin\gamma$ in equations (7a) and (7b) respectively and solving for γ_o and γ gives:

$$\gamma_0 = \tan^{-1}\left(\frac{\frac{w}{r_0}\sin\phi}{1 - \frac{w}{r_0}\cos\phi}\right), \tag{8a}$$

$$\gamma = \tan^{-1}\left[\frac{\frac{w}{r}\sin(\phi+\theta)}{1 - \frac{w}{r}\cos(\phi+\theta)}\right]. \tag{8b}$$

Now equations (8a) and (8b) can be rewritten using the series expression $\tan^{-1}(y) = y - \frac{y^3}{3} + \frac{y^5}{5}$ to give a simple expression for γ_o and γ to second order:

$$\gamma_0 = \frac{\frac{w}{r_0}\sin\phi}{1-\frac{w}{r_0}\cos\phi}, \tag{9a}$$

$$\gamma = \frac{\frac{w}{r}\sin(\phi+\theta)}{1-\frac{w}{r}\cos(\phi+\theta)}. \tag{9b}$$

For $w << r_0$, r, equations (9a) and (9b) may be expanded using $(1+y)^{-1} = 1 - y + y^2 - \ldots$ to give:

$$\gamma_0 = \frac{w}{r_0}\sin\phi\left[1+\frac{w}{r_0}\cos\phi - \left(\frac{w}{r_0}\right)^2\cos^2\phi + \ldots\right], \tag{10a}$$

$$\gamma = \frac{w}{r}\sin(\phi+\theta)\left[1+\frac{w}{r}\cos(\phi+\theta) - \left(\frac{w}{r}\right)^2\cos^2(\phi+\theta) + \ldots\right]. \tag{10b}$$

Expanding $\sin\gamma_0$, $\cos\gamma_0$, $\sin\gamma$ and $\cos\gamma$, keeping terms to second order in γ_0, γ in equation (6) gives:

$$\frac{n\lambda}{d_0+\delta(w)} = \left(1-\frac{\gamma_0^2}{2}\right)\cos\phi - \gamma_0\sin\phi - \left(1-\frac{\gamma^2}{2}\right)\cos(\phi+\theta) + \gamma\sin(\phi+\theta) \tag{11}$$

Using equations (10a) and (10b) in equation (11) and keeping terms to second order in w gives:

$$\frac{n\lambda}{d_0+\delta(w)} = \cos\phi - \frac{1}{2}\left(\frac{w}{r_0}\right)^2 \sin^2\phi\cos\phi - \frac{w}{r_0}\sin^2\phi - \left(\frac{w}{r_0}\right)^2 \sin^2\phi\cos\phi$$
$$-\cos(\phi+\theta) + \frac{1}{2}\left(\frac{w}{r}\right)^2 \sin^2(\phi+\theta)\cos(\phi+\theta) \qquad .(12)$$
$$+\frac{w}{r}\sin^2(\phi+\theta) + \left(\frac{w}{r}\right)^2 \sin^2(\phi+\theta)\cos(\phi+\theta)$$

Dividing through equation (12) by nλ and grouping terms in powers of w gives:

$$\frac{1}{d_0+\delta(w)} = \frac{\cos\phi - \cos(\phi+\theta)}{n\lambda}$$
$$+w\left[\frac{\sin^2(\phi+\theta)}{nr\lambda} - \frac{\sin^2\phi}{nr_0\lambda}\right] \qquad . \qquad (13)$$
$$+w^2\left\{\frac{3}{2}\frac{\sin^2(\phi+\theta)\cos(\phi+\theta)}{nr^2\lambda} - \frac{3}{2}\frac{\sin^2\phi\cos\phi}{nr_0\lambda}\right\}$$

Using the definition $d_0+\delta(w) = d(w)$, we can now identify the line density coefficients from equation (13) to be:

$$a_0 = \frac{\cos\phi - \cos(\phi+\theta)}{n\lambda}, \qquad (14a)$$

$$a_1 = \frac{1}{n\lambda}\left(\frac{\sin^2(\phi+\theta)}{r} - \frac{\sin^2\phi}{r_0}\right), \qquad (14b)$$

$$a_2 = \frac{1}{n\lambda}\left[\frac{3}{2}\frac{\sin^2(\phi+\theta)\cos(\phi+\theta)}{r^2} - \frac{3}{2}\frac{\sin^2\phi\cos\phi}{r_0^2}\right]. \qquad (14c)$$

Choosing appropriate values for θ and ϕ determines the coefficients, or values may be chosen for θ (grazing incidence) and $a_0 = 1/d_0$ to define ϕ so as to allow sufficient dispersion from the grating to meet the monochromater design requirements, thus determining a_1 and a_2. For θ=3.5 degrees, a_0=15000 lines/centimeter, λ=100 angstroms, r_0=285 cm and r=255 cm we find a_1=118.084 lines/cm^2 and a_2=0.689824 lines/cm^3. For θ=5.0 degrees, a_0=6000 lines/cm, λ=200 angstroms, r_0=275 cm and r=245 cm we find a_1=50.1905 lines/cm^2 and a_2=0.310607 lines/cm^3. The above procedure can be used to find corrections to the line space density, σ_o, to any order with diminishing returns for higher orders.

The coefficients above were found by picking a particular wavelength in the region to be covered by the grating. We must now confirm that these results make the focal curves, r(λ), a weak function of wavelength in the region of the spectrum covered by the grating. A complete analytical expression for r(λ) can be found from equations (3), (4), (5a) and (5b) given the line space density, σ, source distance, r_0, and grazing angle of incidence, ϕ. Solving equation (5b) for r gives:

$$r = \frac{w \sin(\phi + \theta + \gamma)}{\sin \gamma}. \tag{15}$$

Solving equation (4) for θ gives:

$$\theta = \cos^{-1}\left[\cos\phi - \frac{n\lambda}{d_0}\right] - \phi. \tag{16}$$

Solving equation (3) for γ gives:

$$\gamma = \cos^{-1}\left[\cos(\phi + \gamma_0) - \frac{n\lambda}{d}\right] - (\phi + \theta). \tag{17}$$

Solving equation (5a) for γ_0 gives:

$$\gamma_0 = \tan^{-1}\left(\frac{\frac{w}{r_0}\sin\phi}{1-\frac{w}{r_0}\cos\phi}\right). \qquad (18)$$

Using equations (16), (17) and (18) in equation (15), the focal curves can be plotted as a function of wavelength. Figures 4 through 9 show the focal curves for the two gratings illustrating the degree of focusing provided by the addition of the linear and quadratic terms in the line space density. Note that the vertical scales are dramatically different for the constant, linear and quadratic terms. These analytical results are confirmed by SHADOW using the *focnew* utility to examine the variation in the vertical waist size of the beam as a function of position along the optical axis.

5.1 Depth of Focus

The figures (4 - 9) show that the actual focal distance can vary from the desired focal distance by as much as ten centimeters depending on the wavelength. To judge the effect of this variation, the depth of focus, defined in figure 10, is calculated using the angles, $\gamma^{\pm}$, for the rays diffracted at either end of the grating. The small angle formula can be used to write:

$$\text{depth of focus} = 2\frac{s}{\theta} = 2\frac{\text{exit slit width}}{\gamma^{+}+\gamma^{-}}. \qquad (19)$$

The depth of focus as a function of wavelength is shown in figures 11 and 12. At 100 angstroms and an exit slit width of 100 microns, the depth of focus is approximately 73.8 cm. At 100 angstroms and an exit slit width of 50 microns,

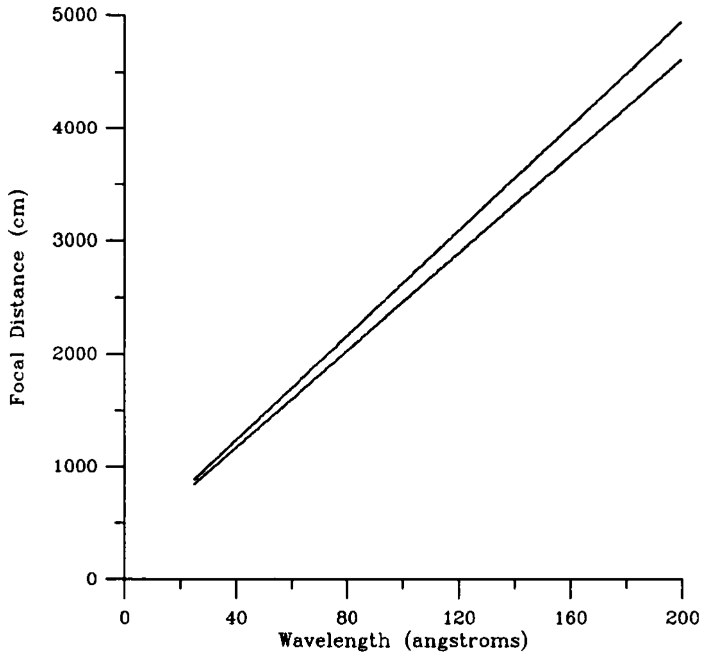

Figure 4. Focal curve for high energy grating with constant line space density, $\sigma = a_0$. Upper curve is for w = -7, lower curve is for w = +7.

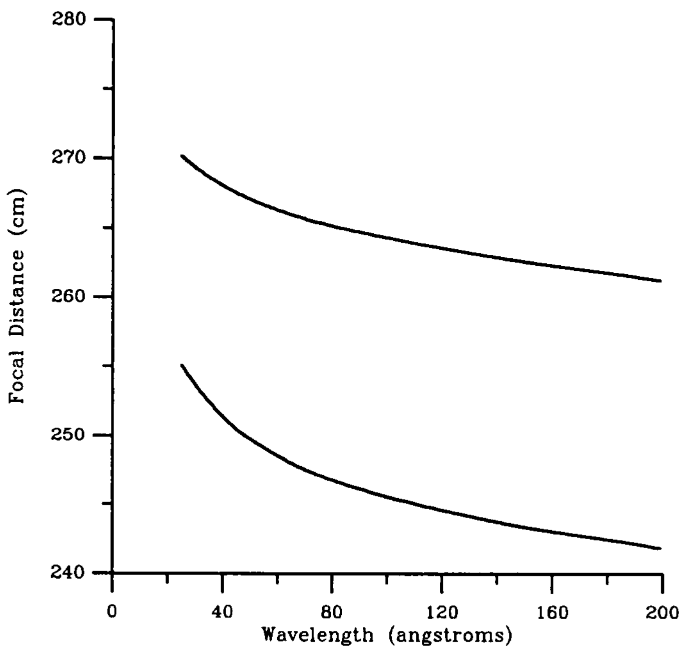

Figure 5. Focal curve for high energy grating with linear variation in the line space density, $\sigma = a_0 + a_1x$. Upper curve is for w = +7, lower curve is for w = -7.

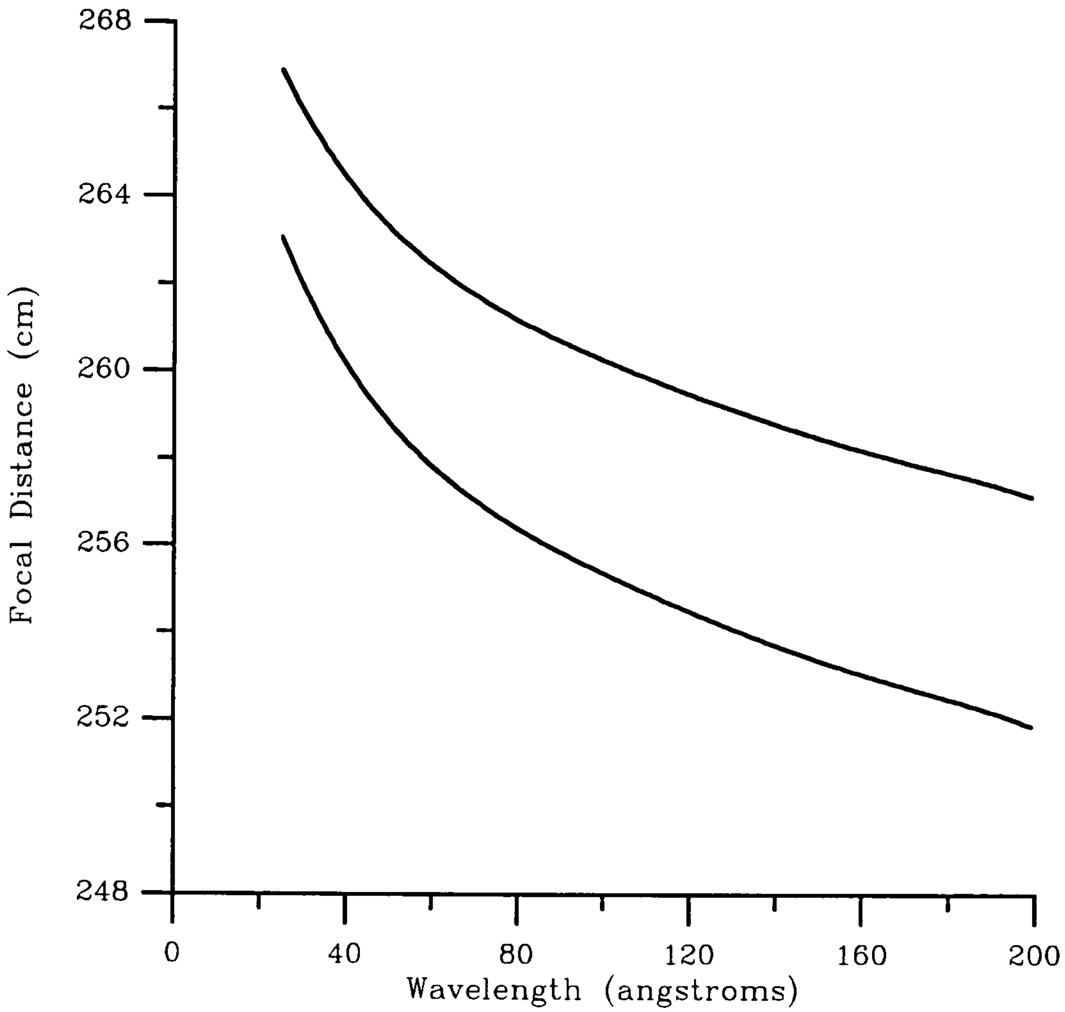

Figure 6. Focal curve for high energy grating with quadratic term added to the line space density, $\sigma = a_0 + a_1x + a_2x^2$. Upper curve is for w = -7, lower curve is for w = +7.

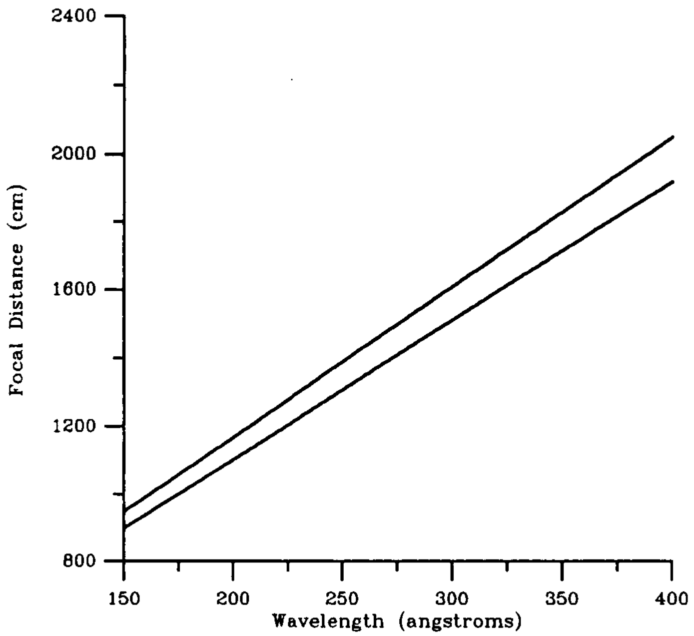

Figure 7. Focal curve for low energy grating with constant line space density, $\sigma = a_0$. upper curve is for w = -7, lower curve is for w = +7.

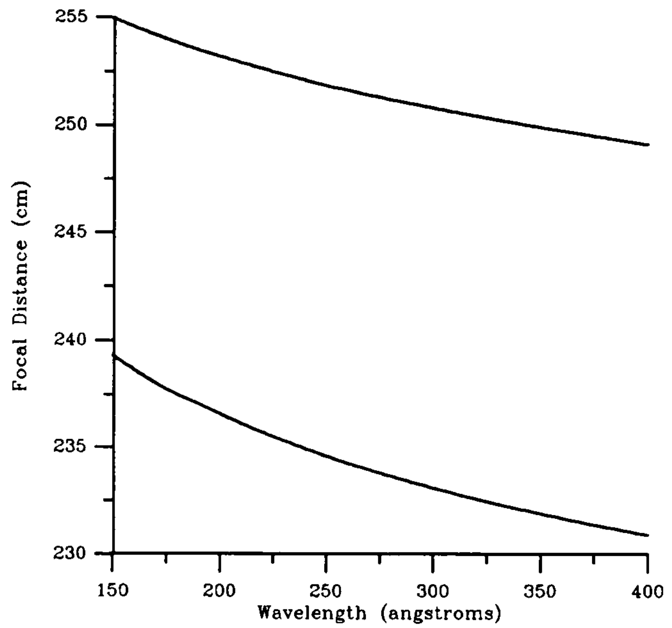

Figure 8. Focal curve for low energy grating with linear variation in the line space density, $\sigma = a_0 + a_1x$. Upper curve is for w = +7, lower curve is for w = -7.

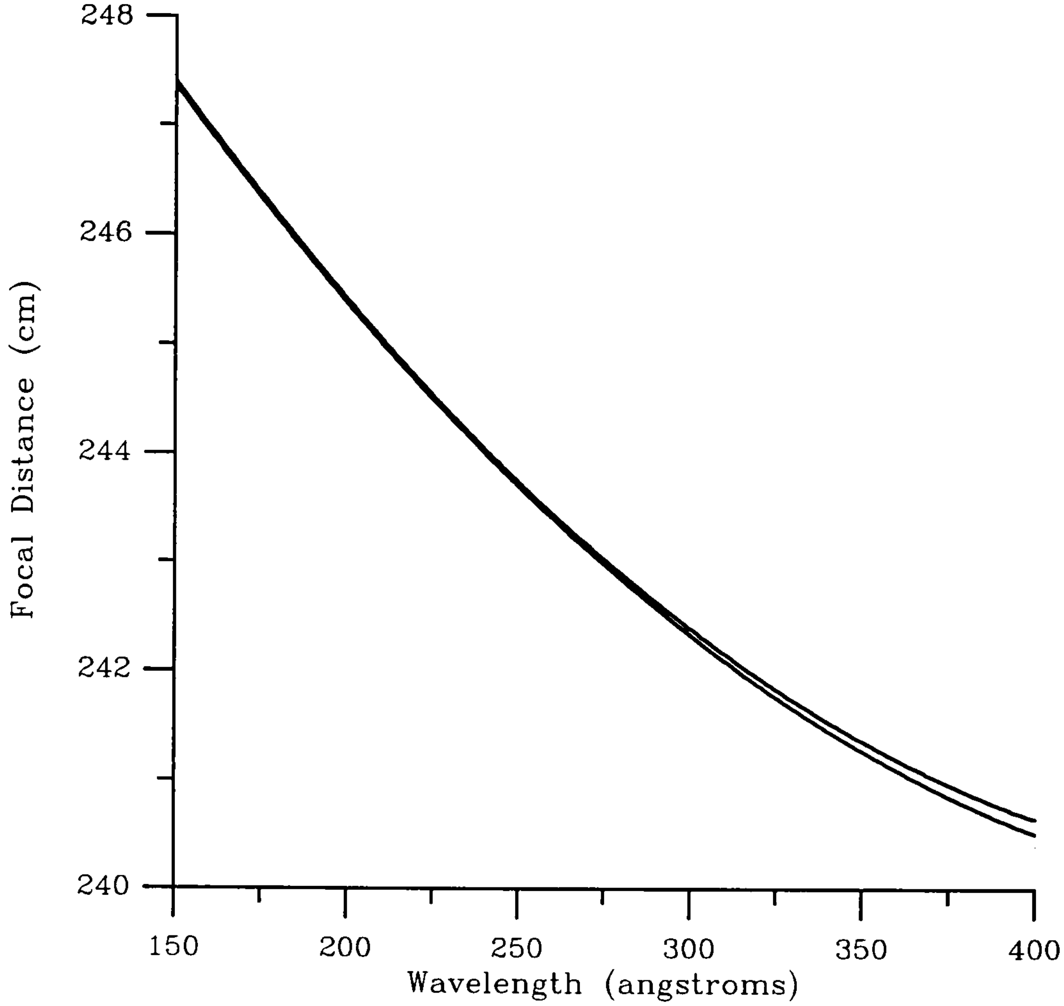

Figure 9. Focal curve for low energy grating with linear and quadratic variation in the line space density, $\sigma = a_0 + a_1x + a_2x^2$. Upper curve is for w = -7, lower curve is for w = +7.

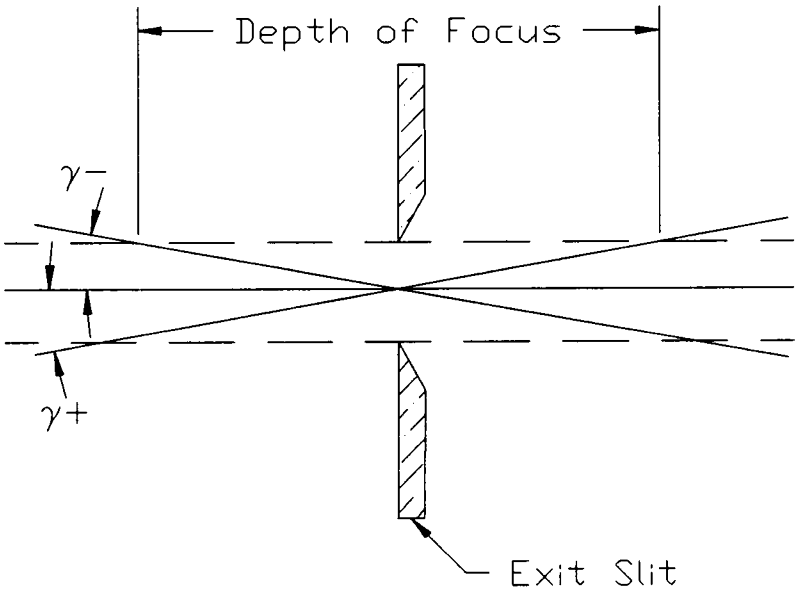

Figure 10. Geometry for depth of focus calculation.

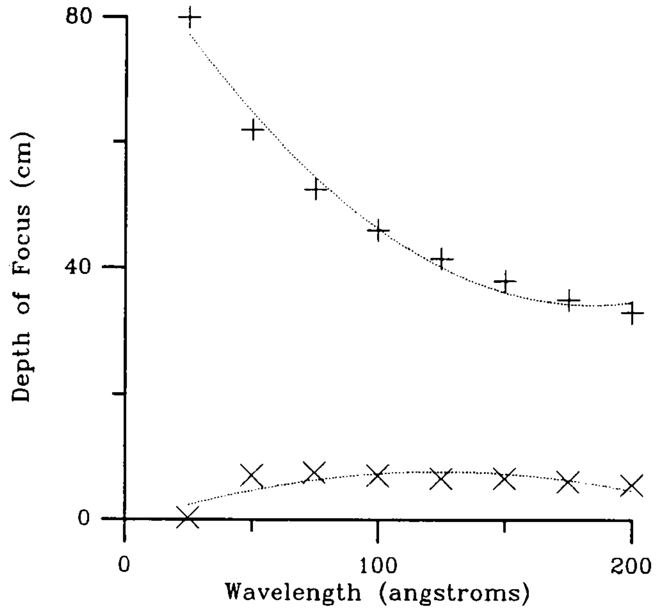

Figure 11. Depth of focus as a function of wavelength for high energy grating. Upper curve is for 0.05 cm exit slit width, lower curve is for 0.01 cm exit slit width.

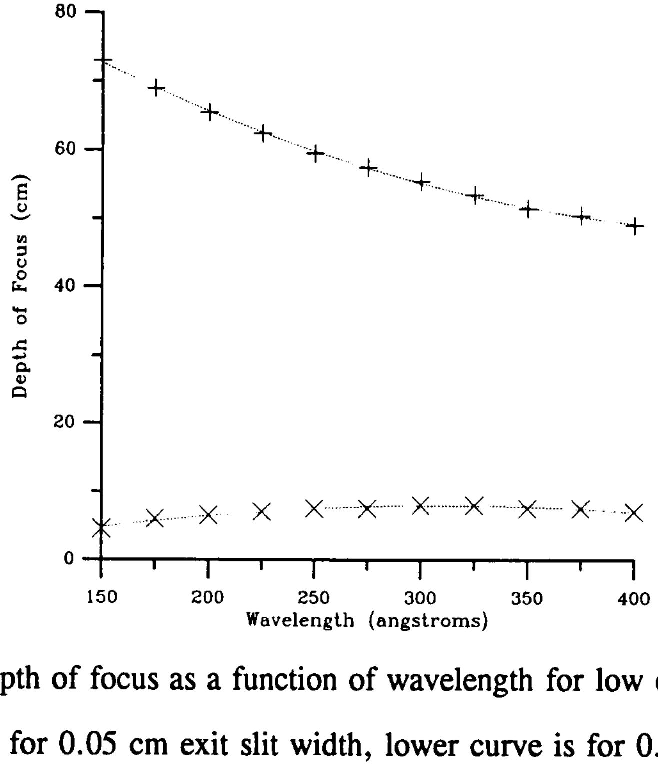

Figure 12. Depth of focus as a function of wavelength for low energy grating. Upper curve is for 0.05 cm exit slit width, lower curve is for 0.01 cm exit slit width.

the depth of focus is approximately 36.9 cm. Results from SHADOW show that the actual depth of focus will be much smaller than that predicted by the simple analytical model. Using the *focnew* utility, the depth of focus at 100 angstroms with an exit slit width of 500 microns is approximately 45 cm. With an exit slit width of 100 microns, the depth of focus is reduced to approximately 10 cm. Thus the resolving power will not be significantly affected by the relatively small variation in focal length.

6. RAY TRACING STUDIES

A complete study of the NIST monochromator design has been made using a computer ray tracing package, SHADOW, run on the University of Tennessee VAX cluster. The NIST bl-7 monochromater design consists of two toroidal focusing mirrors, two interchangeable plane gratings, and a plane scanning mirror (beamline schematics are shown in figures 13 and 14). The first toroid acts as a condensing mirror to re-focus (one to one, $d_i = d_o = 254$ cm) the source on the entrance slit. The reflecting surface is nickel coated on a glidcop blank [22]; the angle of incidence is 3 degrees grazing with an acceptance angle of 20 x 3 mrad in the horizontal and vertical respectively. The second toroid fills the gratings with converging light and focuses the source, in the horizontal (one to one, $d_i = d_o = 325$ cm), at the sample. For this mirror, the materials, angle of incidence and acceptance angle are the same as for the condensing mirror. The two plane gratings are ruled into gold on ULE quartz [23] and together cover the range from 30 to 400 angstroms. The high energy grating is set at a constant grazing angle of incidence of 3.5 degrees and is used in the range from 30 to 150 angstroms. The low energy grating is set at a constant grazing angle of incidence of 5.0 degrees and is used in the range from 150 to 400 angstroms. The two gratings are mounted on a single carriage and are placed in the beam by a vertical displacement. The scanning mirror is gold coated on a ULE quartz blank and moves along a line 4 degrees from the horizontal to scan through the dispersed light from the gratings. Grazing angles of incidence on the scanning mirror range from 3 to 15 degrees.

SHADOW is optimized for studying optical systems with synchrotron sources and includes many analysis routines beyond simply tracing rays through the system. Of particular importance is SHADOW's ability to create the depth

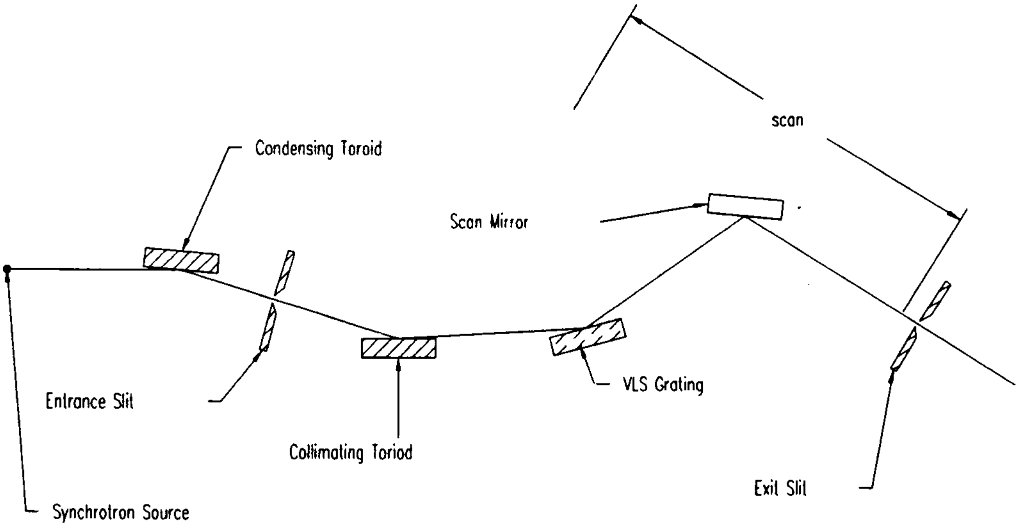

Figure 13. Schematic of NIST bl-7 monochromator showing relative positioning of optical elements and slits. Angles of incidence are exaggerated for clarity.

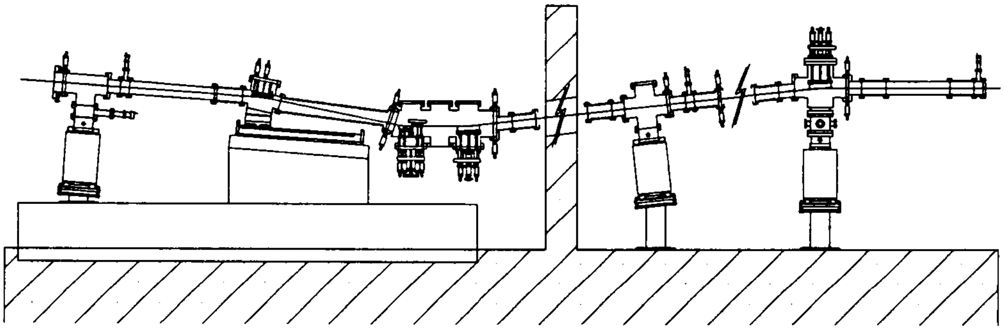

Figure 14. Schematic of NIST bl-7 monochromator showing relative positioning of optical elements and vacuum components.

of the source. Preprocessing (before tracing) routines are available to create models of sources from insertion devices. SHADOW uses a stochastic method to generate photons whose characteristics are dictated by a distribution law and the physical parameters of the electron storage ring. For each ray, SHADOW can calculate up to nineteen coordinates. These are: three spatial coordinates to specify the ray position, three angular coordinates to specify the ray direction, a flag that can be set to indicate when a ray misses an element or its propagation is blocked, the wave number ($2\pi/\lambda$), a ray ID number, three coordinates in the ray phase space to allow for coherence and polarization effects, and six coordinates to represent the two polarization directions for the three spatial directions of the photon's electric field vector. The scaling relationship between the number of photons created by SHADOW and that of a real source is linear, thus making it easy to evaluate losses in the optical system.

The parameters of the optical system under investigation, including the source specifications, are initially entered into SHADOW via a series of prompts to the user. The values entered for the NIST bl-7 monochromator are listed in table 2. An attractive feature of the SHADOW package is that the mirror parameters (radii of curvature, dimensions, etc.) can either be entered by the user or SHADOW can calculate the optimal parameters given the user-specified focal plane positions. Mirror parameters returned by SHADOW are listed in table 3. After the system has been entered, individual parameters for each optical element can be changed or reviewed through a menu driven interface. A graphics utility, *plotxy*, is included so that the beam characteristics can be viewed at any point in the system. Any two of eighteen ray variables (only the flag variable is not available for *plotxy*) can be plotted against each

Table 2. Source parameters entered into SHADOW.

SHADOW Prompt	Value Entered
Depth of source	synchrotron
Angle distribution of source	synchrotron
Horizontal half-divergence	10 mrad
Vertical half-divergence	1.5 mrad
Electron orbit radius	83.8 cm
Beam energy	284 MeV
Polarization	Synchrotron, parallel

Table 3. Optical system parameters entered into SHADOW and results of SHADOW computations.

SHADOW prompts	NIST bl-7 Value	
Condensing Mirror		
Surface figure	toroidal	
Element type	reflector	
Reflectivity	full polarization	
mirror dimensions	5 x 14 cm	
Source plane distance	254 cm	
Image plane distance	254 cm	
Incidence angle	87 degrees	
Mirror parameters	internal (computed by SHADOW)	
Focal planes at continuation planes?	yes	
Results of SHADOW computations		
Major radius	4853.259942761540 cm	
Minor radius	13.29333288570773 cm	
Collimating Mirror		
Surface figure	toroidal	
Element type	reflector	
Reflectivity	full polarization	
Mirror dimensions	7 x 20 cm	
Source plane distance	325 cm	
Image plane distance	20 cm	
Incidence angle	87 degrees	
Mirror parameters	internal (computed by SHADOW)	
Focal planes at continuation planes?	no	
Objective focus	325 cm	
Image focus	325 cm	
Results of SHADOW computations		
Major radius	6209.879848021655 cm	
Minor radius	17.00918577895674 cm	
Gratings	High Energy	Low Energy
Surface figure	plane	plane
Element type	reflector, grating	reflector, grating
Reflectivity	full polarization	full polarization
Order	-1	-1
Automatic tuning	yes	yes
Mount type	const. incidence	const. incidence
Ruling coefficients		
zero order	15000	6000
first order	118.084	50.1905
second order	0.689824	0.310607
Mirror dimensions	6 x 14 cm	6 x 10 cm

other. Examples from the NIST bl-7 monochromator are shown in figures 15 through 22.

Most useful for monochromator design is the analysis routine, or post-processor, called *slits*. After removing any slits or apertures and retracing the system, a run of *slits* allows the user to specify the locations of entrance and exit slits and their respective starting width, ending width and step size. *Slits* outputs a file containing the following information for each possible combination of entrance and exit slit widths; entrance slit width, exit slit width, minimum wavelength (or energy) through the exit slit, maximum wavelength through the exit slit, mean wavelength through the exit slit, standard deviation on wavelength through the exit slit, number of good rays, and the average intensity of the electric field through the exit slit.

6.1 Resolving Power

Provided that the wavelength spread through the exit slit assumes a Gaussian distribution, as it does in the NIST BL-7 design (see figure 23), the standard deviation is a good indication of the resolving power of the instrument. Some care must be taken in preparing the source characteristics for resolving power studies. If the source is defined to have a distribution in wavelength that is too large, very few rays will be passed at the exit slit and there will be too few data points to accurately determine the standard deviation. Conversely, if the source wavelength distribution is tuned too narrowly, the resolving power will be artificially high. The source spectrum is easily altered by use of the post-processor *recolor*. The SHADOW manual suggests that the source be tuned to a more narrow band if more than seventy percent of the rays are lost at

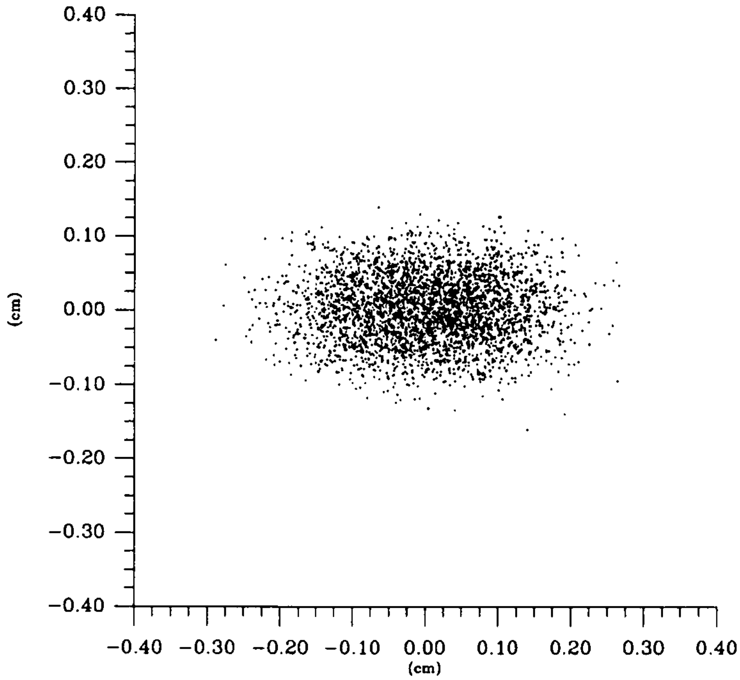

Figure 15. Example of beam profile from SHADOW at source.

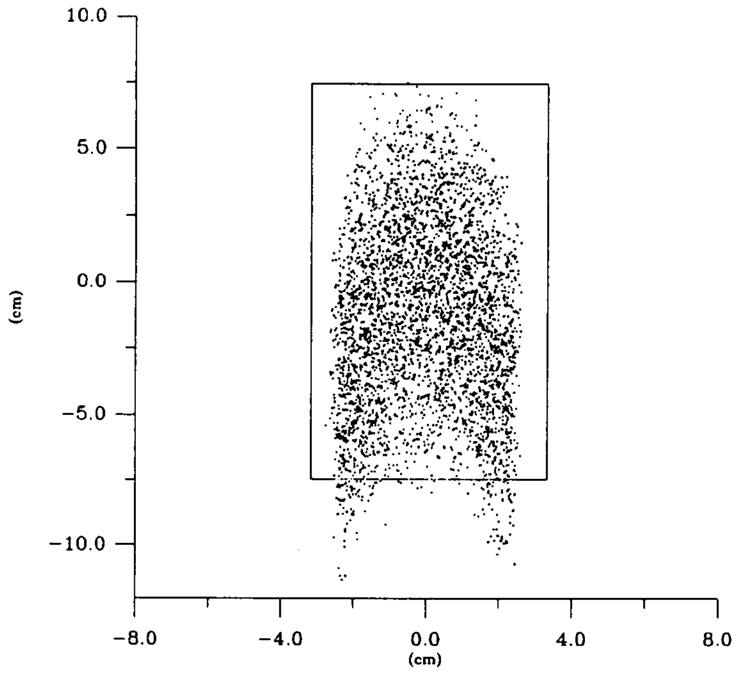

Figure 16. Example of beam profile from SHADOW; footprint on the condensing mirror.

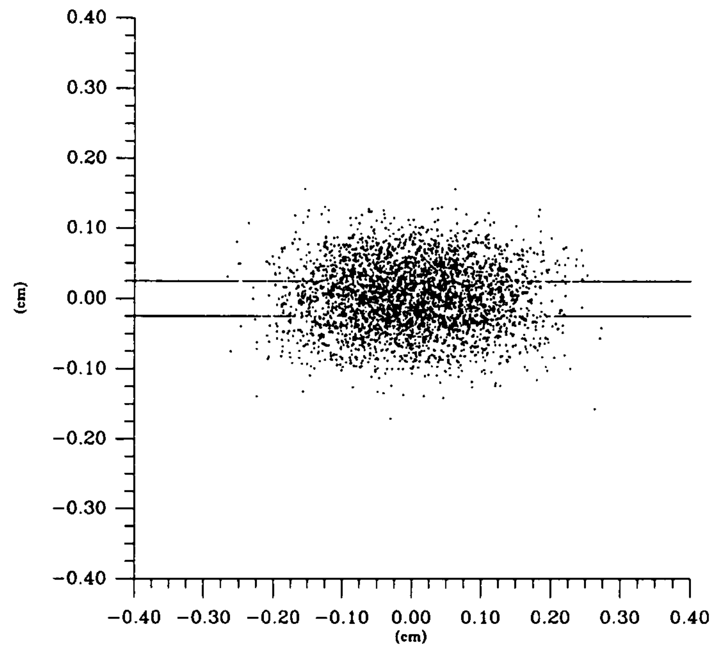

Figure 17. Example of beam profile from SHADOW; image at entrance slit. Horizontal lines show relative width of 0.05 cm entrance slit.

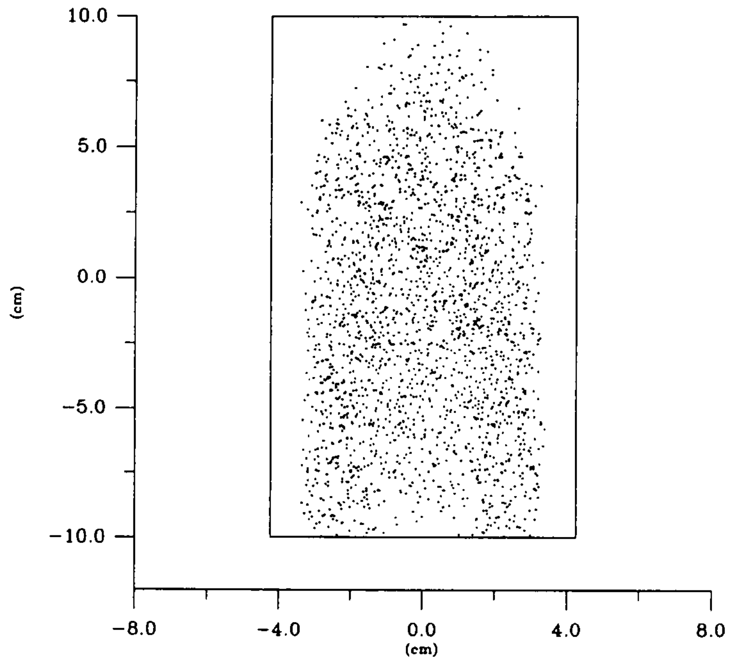

Figure 18. Example of beam profile from SHADOW; footprint on the collimating mirror.

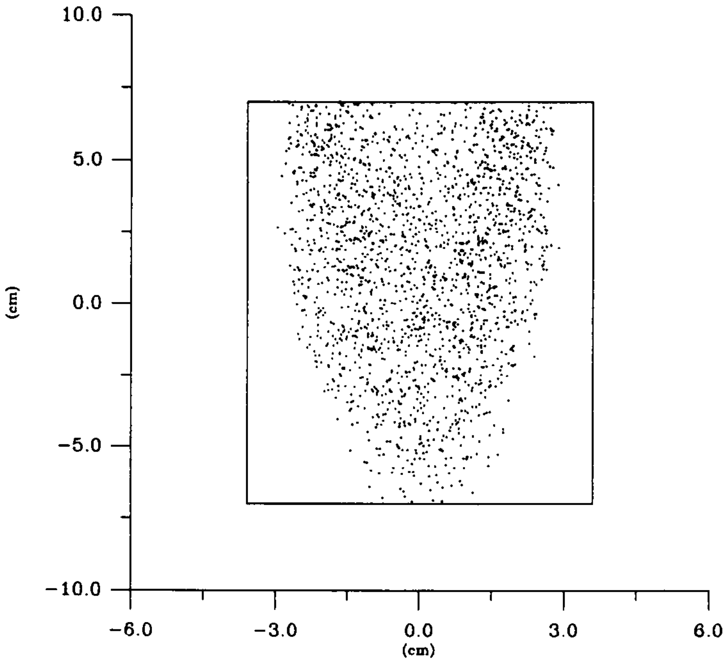

Figure 19. Example of beam profile from SHADOW; footprint on high energy grating.

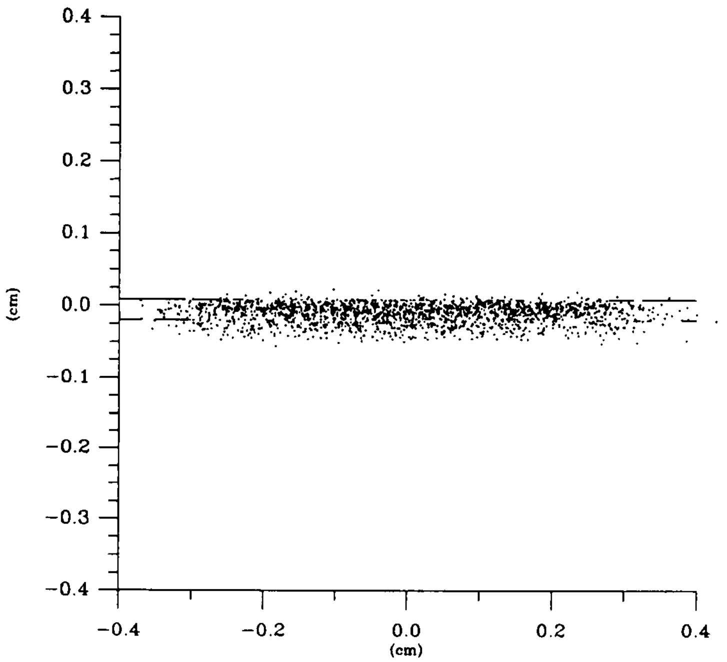

Figure 20. Example of beam profile from SHADOW; image from high energy grating. Horizontal lines show relative width of 0.02 cm exit slit.

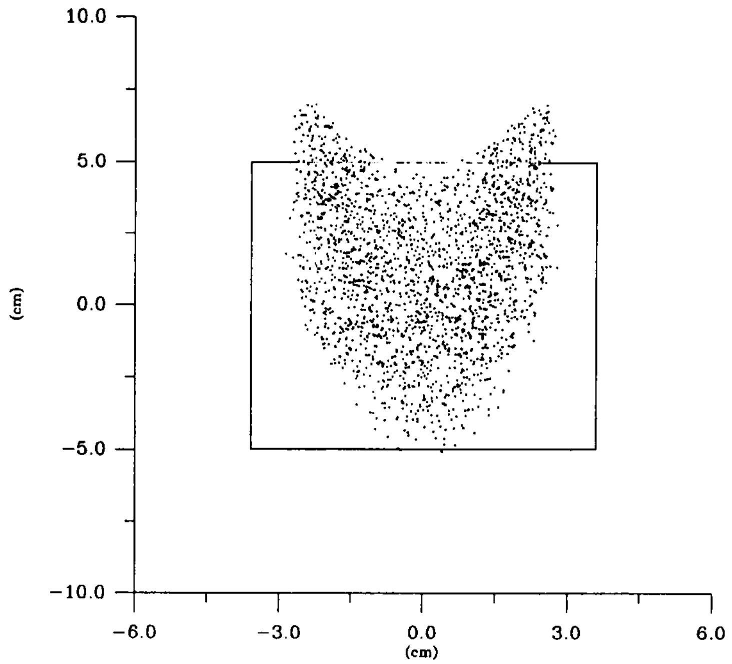

Figure 21. Example of beam profile from SHADOW; footprint on low energy grating.

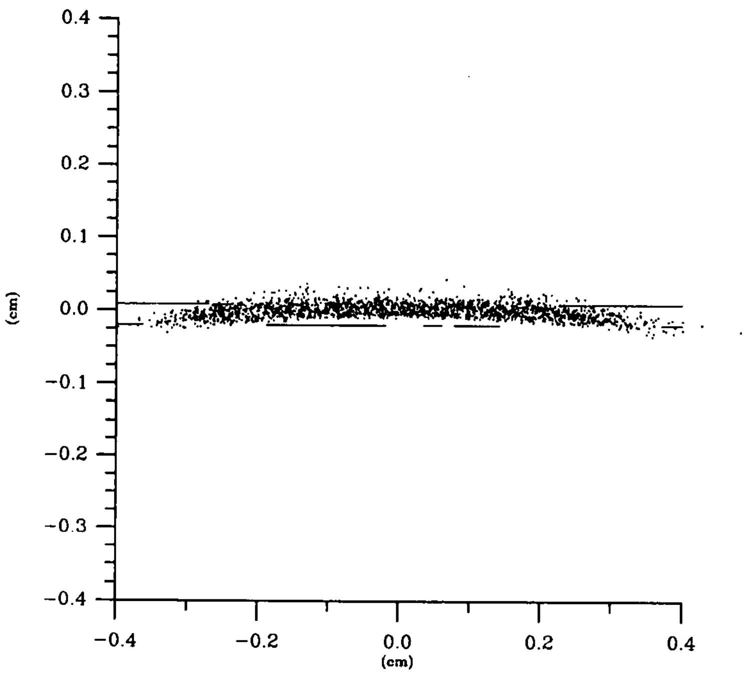

Figure 22. Example of beam profile from SHADOW; image from low energy grating. Horizontal lines show relative width of 0.02 cm exit slit.

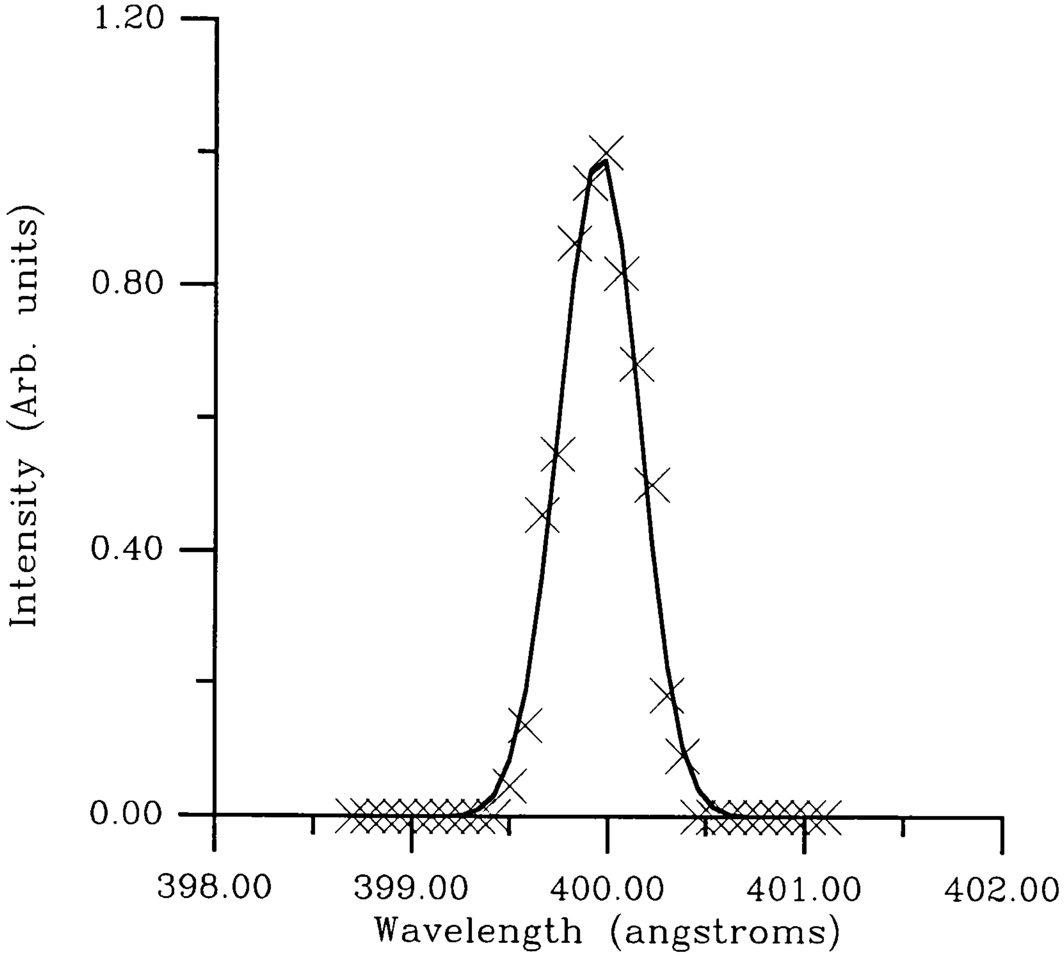

Figure 23. NIST bl-7 monochromator ray trace output at 400 Å, 0.01 cm exit slit width, showing Gaussian distribution of wavelength through exit slit.

the exit slit. Keeping this in mind, the following procedure was used to tune the source:

1. *recolor* source to some best guess spread in wavelength
2. tune grating to central wavelength
3. trace with 500μm entrance slit, note number of good rays at grating
4. remove entrance slit
5. retrace system
6. run *slits*
7. did thirty percent of good rays at grating survive at 500μm exit slit?
    8. if yes, are the minimum and maximum wavelength through larger and smaller, respectively, than the minimum and maximum wavelength of the source?
        if yes, keep this data from *slits*
        if no, re-tune source and goto 5.

With the source correctly tuned, the values of the standard deviation can be tabulated and used to calculate the resolving power of the instrument. To make this calculation, we need the full width at half maximum (FWHM) of a Gaussian function. For a Gaussian normalized to one at maximum we can use:

$$e^{-\frac{x^2}{2\sigma^2}} = \frac{1}{2}$$
$$x = \sigma\sqrt{-2\ln(1/2)} \tag{20}$$

to find the half width in terms of the standard deviation, σ. The FWHM is then given by:

$$FWHM = 2x = 2\sigma\sqrt{-2\ln(1/2)} = 2.35482\sigma. \tag{21}$$

Resolving powers for the NIST BL-7 monochromator, as a function of both slit width and wavelength, are shown in figures 24 and 25. Note that the resolving

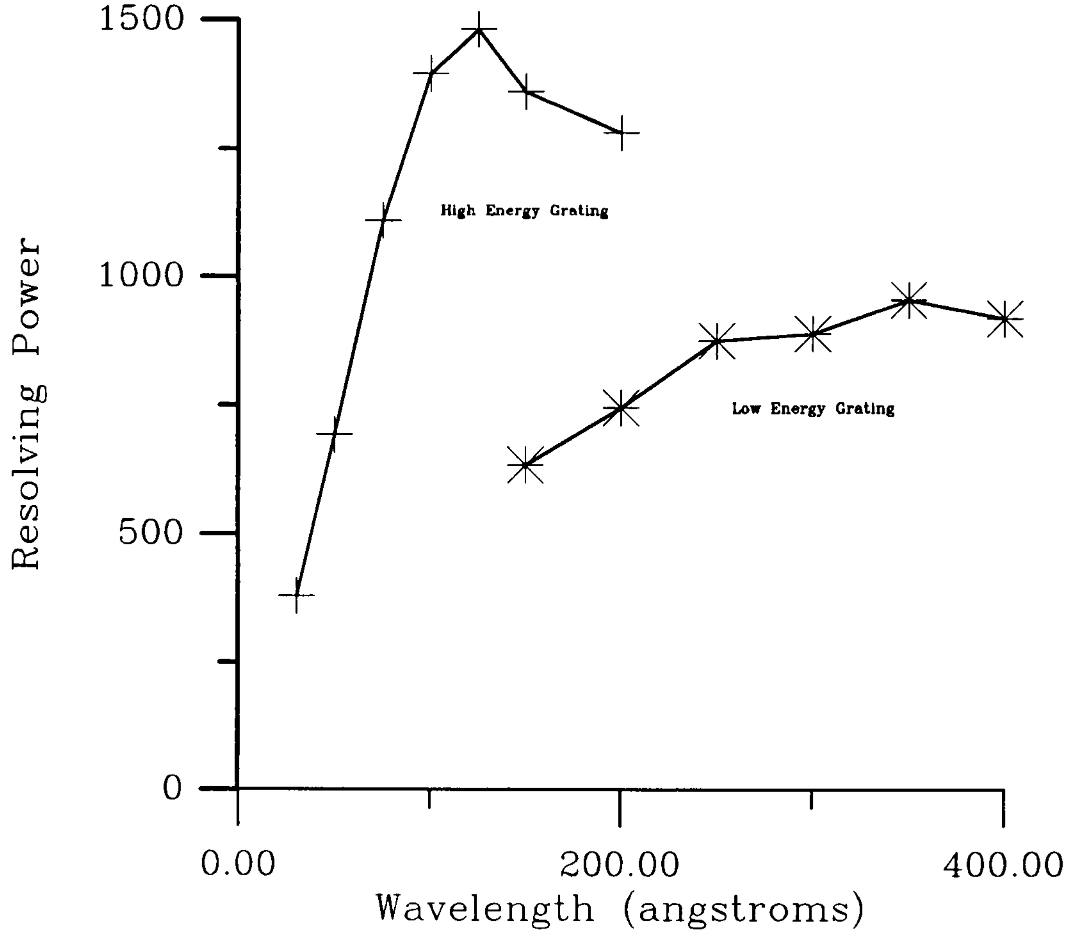

Figure 24. Predicted resolving power of NIST bl-7 monochromator as a function of wavelength.

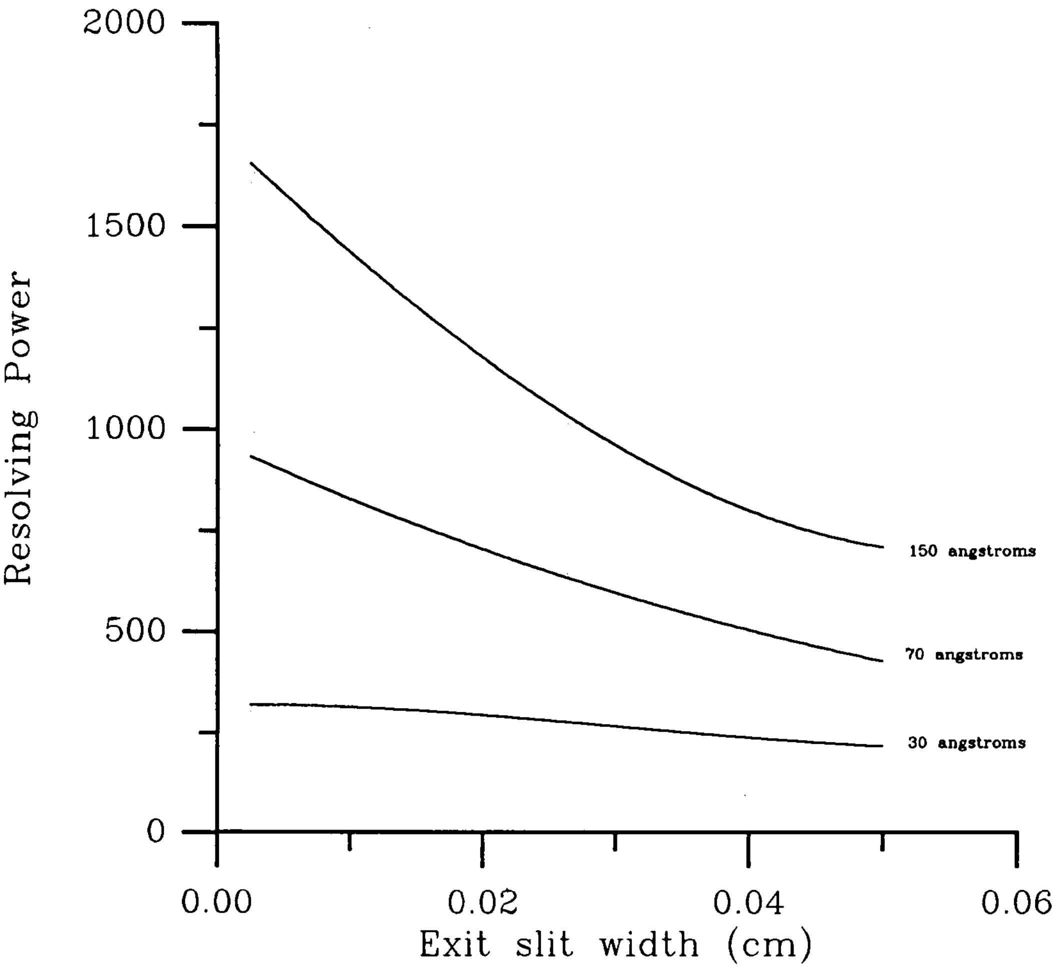

Figure 25. Predicted resolving power of NIST bl-7 monochromator, with high energy grating, as a function of exit slit width.

power at 30 angstroms is much lower than the resolving power at 100 and 150 angstroms. This is not unexpected in light of the focal curves from the section 5. The 30 angstrom light is focused about seven centimeters before the exit slit, whereas the 150 angstrom light is focused only two centimeters after the exit slit.

An important conclusion that can be drawn from the *slits* data is that the entrance slit width has little effect on resolving power in the expected, typically high throughput, mode using entrance slit widths from 200 to 500 micrometers. In general, the resolving power of a monochromator will increase as the entrance slit width decreases. This is because the monochromator optics form an image of the entrance slit at the exit slit and the grating disperses the light into multiple images as a function of wavelength. If the grating does not disperse two wavelengths, or lines, by a vertical distance that exceeds the vertical height of the entrance slit image, the two images overlap. This overlap allows rays from one line to pass through the exit slit when the grating is tuned for the other line, thus reducing the resolving power. A smaller entrance slit image will overcome this problem. However, it is seen in the NIST bl-7 design that a smaller entrance slit does not significantly increase the resolving power of the instrument (see figure 26) over the typical operating range of entrance slit widths. Ray tracing studies of the imaging properties of the toroidal mirrors shows that the size of the entrance slit image is limited by the aberrations introduced by the mirrors (see figures 27 and 28).

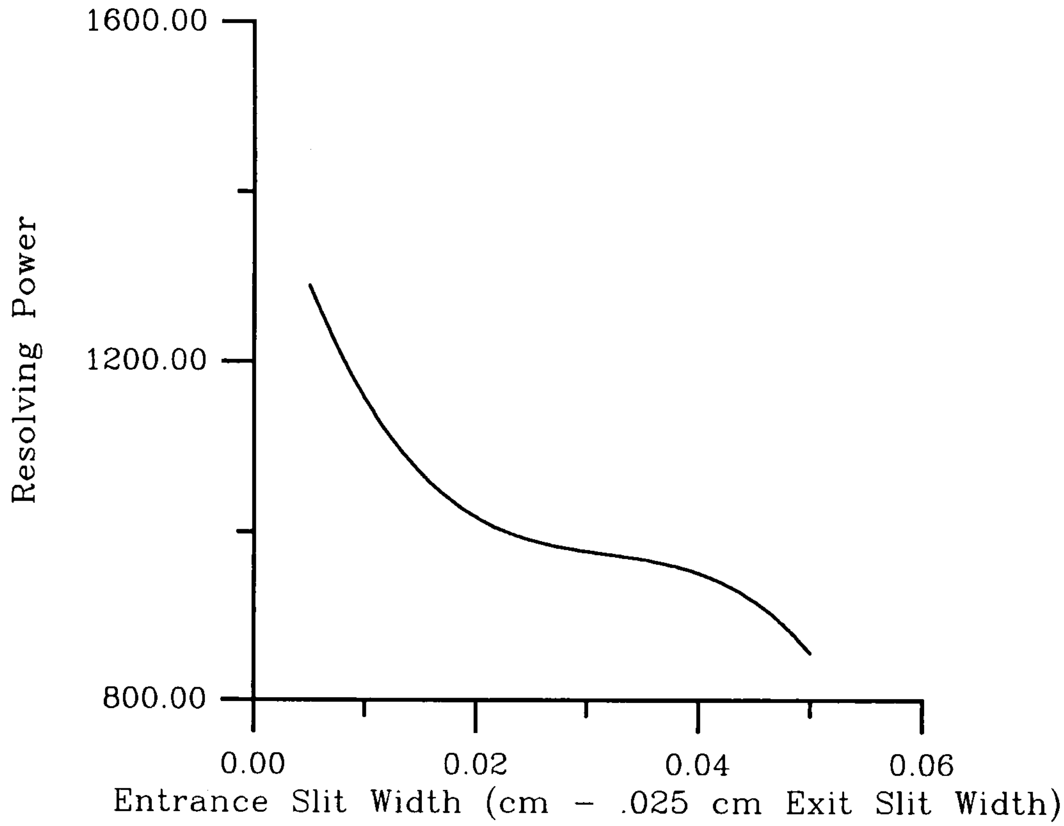

Figure 26. Predicted resolving power of NIST bl-7 monochromator, at 100 Å and 0.025 cm exit slit width, as a function of entrance slit width.

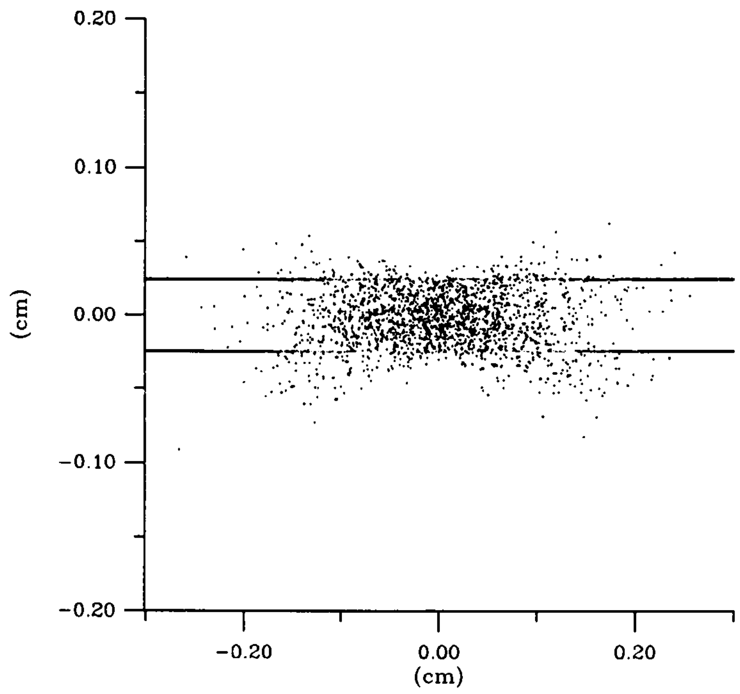

Figure 27. Image of 0.05 cm entrance slit formed by condensing mirror and collimating mirror. Horizontal lines show relative slit width.

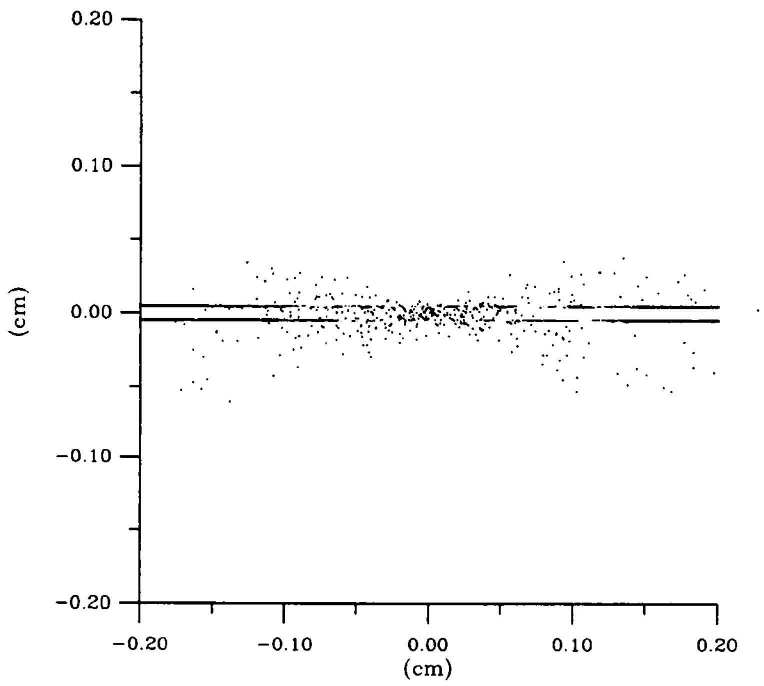

Figure 28. Image of 0.01 cm entrance slit formed by condensing mirror and collimating mirror. Horizontal lines show relative slit width.

6.2 Losses and Throughput

Geometrical losses in the system are easily evaluated by use of the *plotxy* graphics utility and the ray flag variable. Because of its placement at a focal point, the entrance slit acts as a spatial filter (see figure 17). Of the rays that pass through the entrance slit, almost all survive to the exit slit, where significant losses occur due to dispersion from the grating. Geometrical loss results from SHADOW, beginning with 5000 rays at the source, (100 angstroms) are: 239 rays are lost at the condensing mirror, 2704 rays are lost at an entrance slit width of 500 μm, 13 rays are lost at the second toroid, 15 rays are lost at the grating and 797 rays are lost at an exit slit width of 100 μm. Thus the system has an efficiency of about 25 % when only geometrical losses are considered.

Given the density of an element, SHADOW can calculate a variety of optical constants for optical elements in the system (optics utility *abrefc*). Taking into account the polarization dependence of the reflectivity (again at 100 angstroms), results from SHADOW are: condensing mirror 75% efficiency, second toroid 79% efficiency, grating 88% efficiency. Adding geometrical losses to these results gives an overall system efficiency at 100 angstroms of about 14%. Additional losses at the scanning mirror reduce this to about 10% efficiency at 100 angstroms.

6.3 Alignment Errors

During assembly, questions arose as to how the angle of incidence on the gratings affects their focusing properties. Figure 29 shows how the grating's focal distance changes with angle of incidence for various wavelengths. These analytical results are confirmed by SHADOW using *focnew*. Since the focal distance does not change dramatically with incidence angle, it is expected that the resolving power will not be significantly affected for small variations in the angle of incidence. This is confirmed by ray tracing using the previously described method to predict resolving power.

An additional feature of the SHADOW program is the ability to move any element from its original position, in three dimensions, allowing the user to evaluate the effects of alignment errors. An investigation of the NIST bl-7 system's sensitivity to the grating yaw adjustment revealed that alignment errors as small as one degree would result in a horizontal deflection of the first-order light by as much as four centimeters. This deflection is not seen for the zero-order light because the higher-orders are diffracted perpendicular to the grating rulings whereas the zero-order light is simply reflected according to Snell's law.

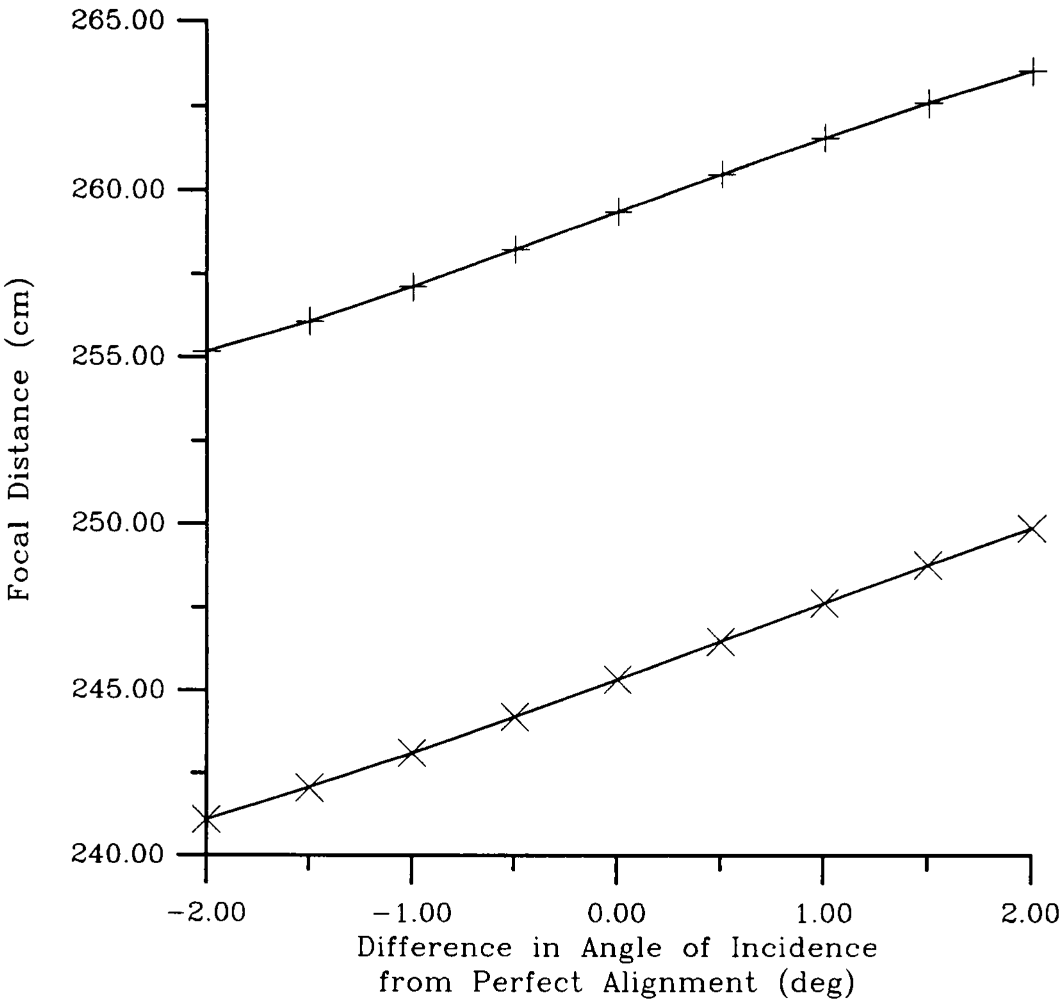

Figure 29. Effect of angle of incidence on grating focal distance. Upper curve is for high energy grating, lower curve is for low energy grating.

7. EXPERIMENTAL EVALUATION

7.1 Experimental Procedure

Before measuring the resolving power and throughput of the NIST bl-7 monochromator, the system was aligned using the zero-order visible light. The procedure began at the optical element closest to the storage ring and progressed along the length of the beamline. First, the best stigmatic focus of the condensing mirror was found. Small adjustments to the position of the entrance slit were made to place it at the focal point of the condensing mirror. The position of the collimating mirror was adjusted until the reflecting surface was filled by the incident light from the entrance slit. Fine adjustments were then made to this mirror's orientation until the best stigmatic focus was produced at a distance of 325 cm on the horizontal from the mirror center. For each grating, the angle of incidence was set by measuring the angle of reflection of the zero-order light from the collimating mirror and the manipulator setting recorded. A HeNe laser was used to set the grating yaw position insuring that the rulings were perpendicular to the optical axis. The orientation of the scanning mirror was then set by adjusting the angle of incidence of a grating so that the zero-order light was reflected at the same angle as some conveniently chosen wavelength in first-order. This was repeated for a wavelength position at either end of the scanning mirror's travel to set the mirror's line of travel parallel to the beam. Finally, small adjustments were made to the position of the exit slit to place it at the specified position of 25 cm before the focal point of the collimating mirror. After extensive baking of the vacuum chambers, fine adjustments were made with the system under vacuum.

The resolving power of the monochromator has been measured by recording transmission spectra near the absorption edges of Al, Be, C and Si thin films (500 - 1500 angstrom thickness). The Al, Be and C filters are mounted in a holder on a UHV compatible feedthrough about 25 cm behind the entrance slit and are positioned in the beam by vertical translations. Positioning of the scanning mirror is accomplished by a Macintosh II computer interfaced with a Compumotor 4000 motion controller via a general purpose interface board (GPIB). The model 4000 in turn controls a precision linear rail table and a UHV compatible feedthrough using microstepping motors and absolute encoders. The rail table sets the position of the scanning mirror along the beamline to select the desired wavelength. The feedthrough sets the angle of the scanning mirror to reflect the light onto the exit slit. The spectra are recorded using the computer to monitor the current output of a photodiode mounted about 25 cm behind the exit slit. The Si filter is mounted just above the surface of the photodiode.

7.2 Results

The spectra shown in figures 30 through 34 were recorded while the monochromator scanned across the absorption edge of each filter. The derivative of the spectra was taken and a Gaussian curve was fit to the derivative to find the standard deviation on wavelength. From this standard deviation, the resolving power was calculated as described in equations (20) and (21). The measured resolving power as a function of wavelength and as a function of exit slit width are shown in figures 35 and 36. Due to the broad linewidths of these solids at room temperature[24-27], direct measurements of

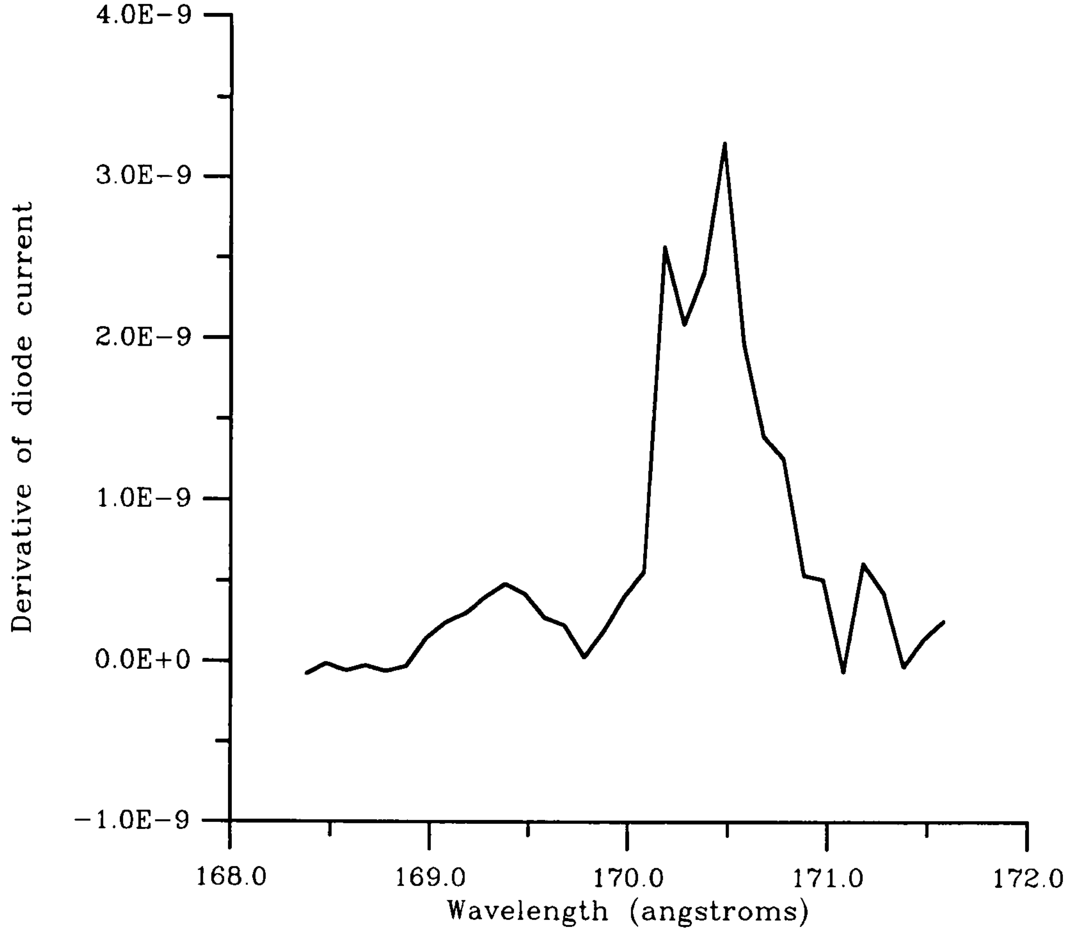

Figure 30. Aluminum absorption edge using low energy grating. Note two peaks around 169.5 Å and 170.5 Å showing spin orbit splitting.

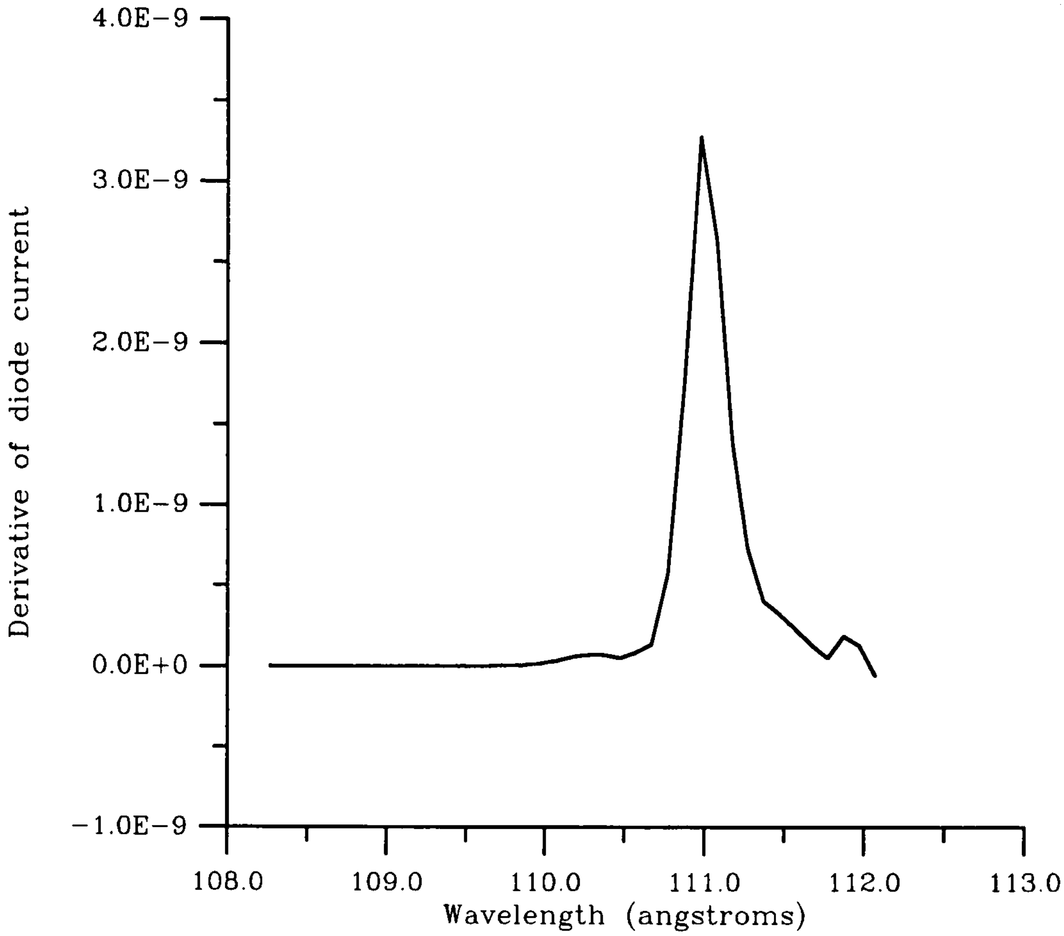

Figure 31. Beryllium absorption edge using high energy grating.

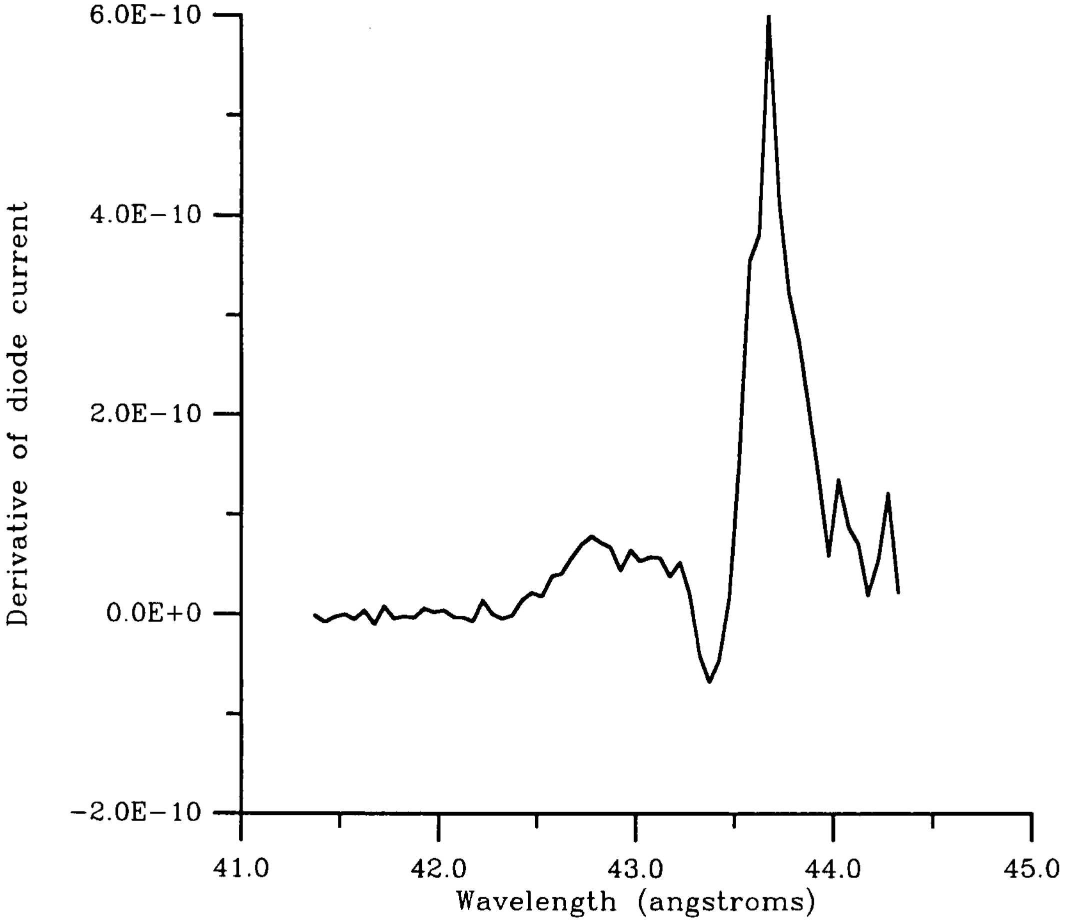

Figure 32. Carbon absorption edge using high energy grating.

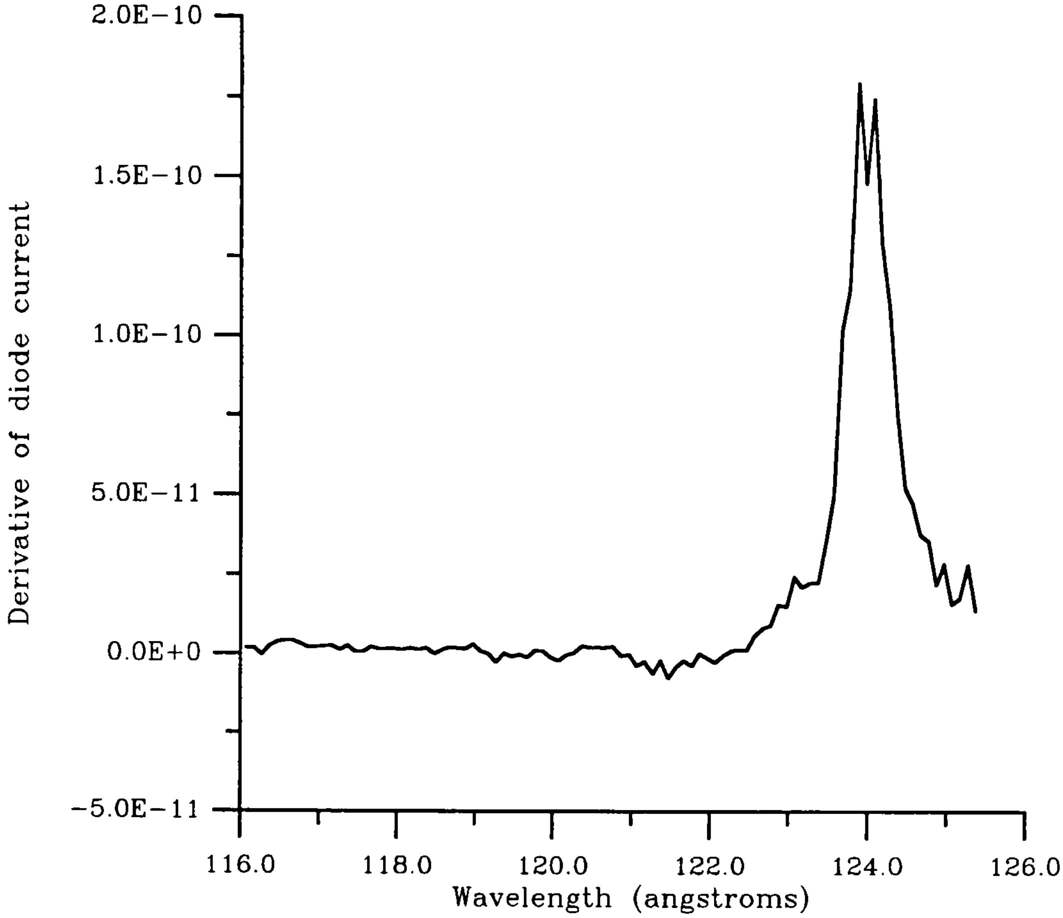

Figure 33. Silicon absorption edge using low energy grating.

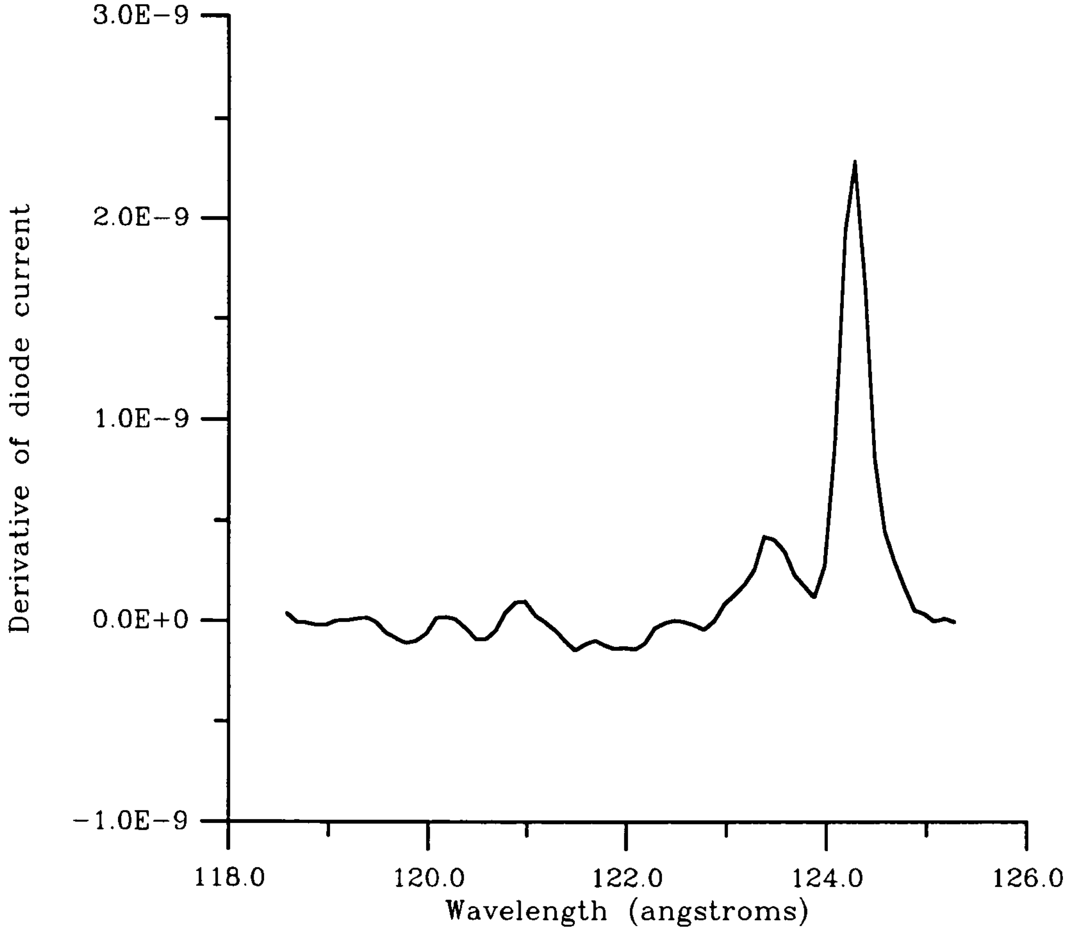

Figure 34. Silicon absorption edge using high energy grating. Note the two peaks around 124 Å showing spin orbit splitting.

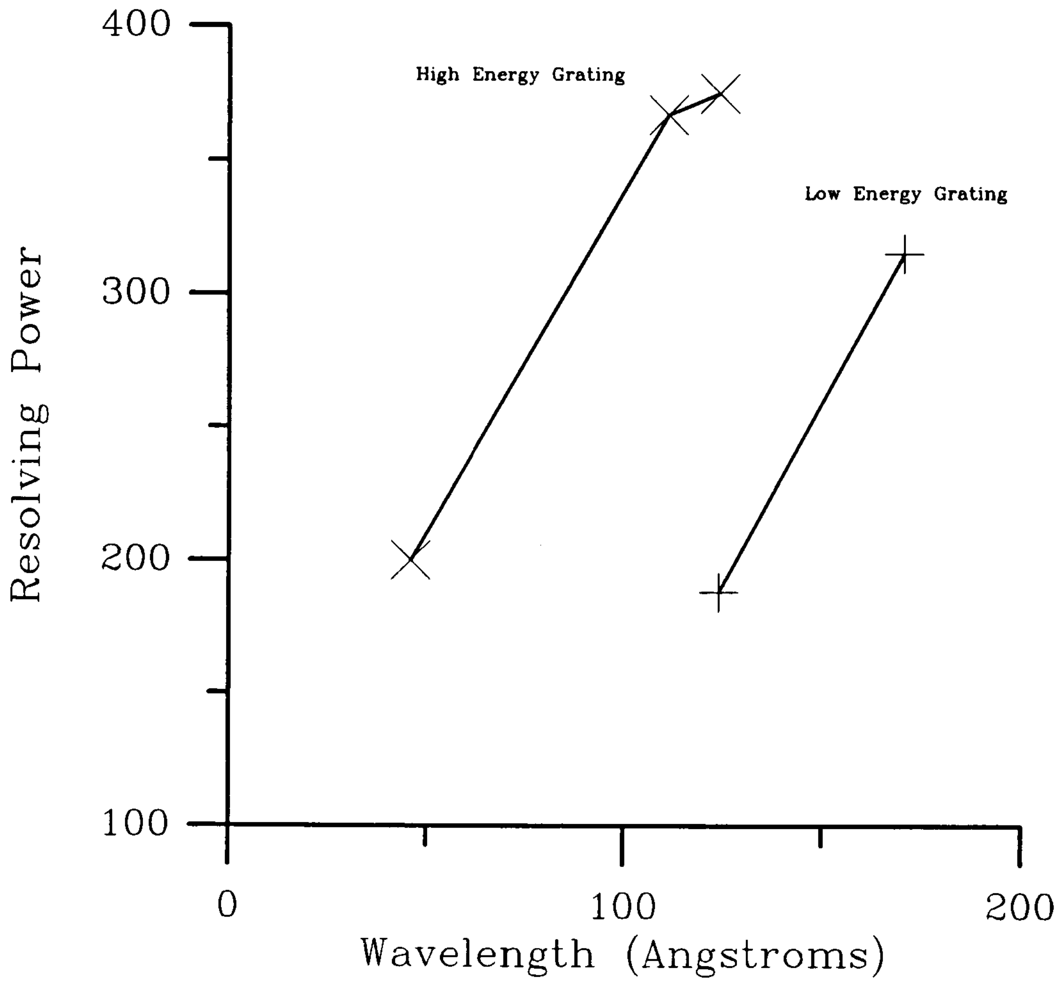

Figure 35. Measured resolving power of NIST bl-7 monochromator shown as a function of wavelength.

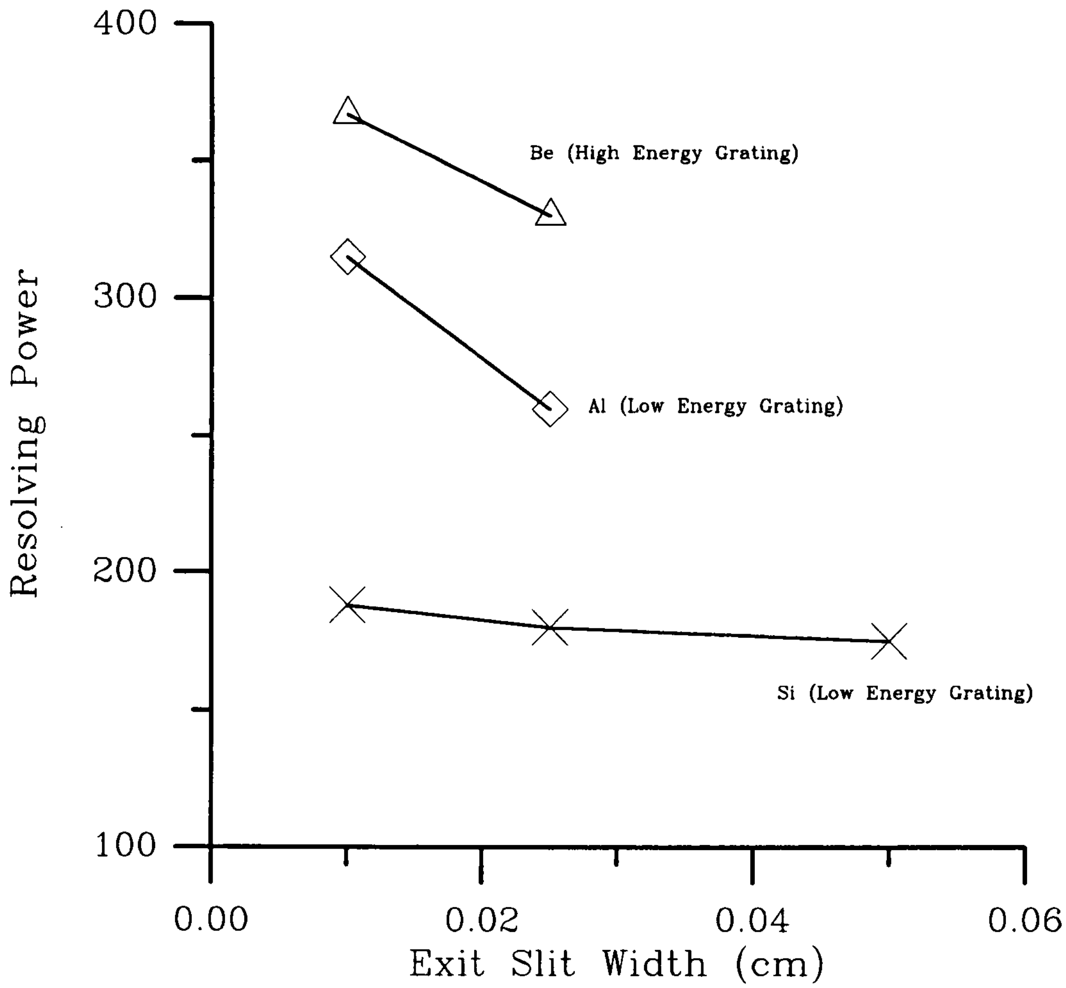

Figure 36. Measured resolving power of NIST bl-7 monochromator shown as a function of exit slit width.

resolving power were limited to values no greater than about 400. The largest measured resolving power was 375, made by using the Si L_{III} edge at 124 angstroms. Figures 30 and 34 show that the spin-orbit splitting at the Al L_{II-III} edge and the Si_{II-III} edge are well resolved. Thus it is concluded that resolving powers in excess of 400 have been achieved.

A second method has been used to find the instrument resolving power at the Si L_{III} edge by comparing the NIST bl-7 data to a similar study of the Si absorption edge using electron energy loss spectroscopy (EELS) [28]. Data from EELS has been made available, in electronic form (see figure 37), by private communication from Charles Tarrio, National Institute of Standards and Technology, Gaithersburg, Maryland. The EELS data was recorded with an instrument resolving power on the order of 1500, hence instrument broadening effects are negligible for the relatively broad Si edge. Comparison of the NIST bl-7 data to the EELS data reveals a slight broadening of the Si edge from the NIST monochromator. The linewidth is broadened by the instrument so that the measured linewidth is the convolution of two functions: the shape of the Si edge itself and the instrument function. Assuming both the Si edge and the instrument function have Gaussian form, the instrument function can be calculated using the EELS data as a measure of the Si edge line width. It can be shown (see appendix) that the convolution of two Gaussian functions, $G_1(x)$ and $G_2(x)$, is another Gaussian function, $G_R(x)$, with $\sigma_R^2 = \sigma_1^2 + \sigma_2^2$, where σ_R and σ_1 are found from Gaussian curves fit to the NIST data and the EELS data respectively. A simple calculation gives $\sigma_2 = 0.07228$ for the instrument function. Using this value of σ_2, the instrument resolving power is calculated to be 730 at 124 angstroms. Although unable to fully test the limits of predicted

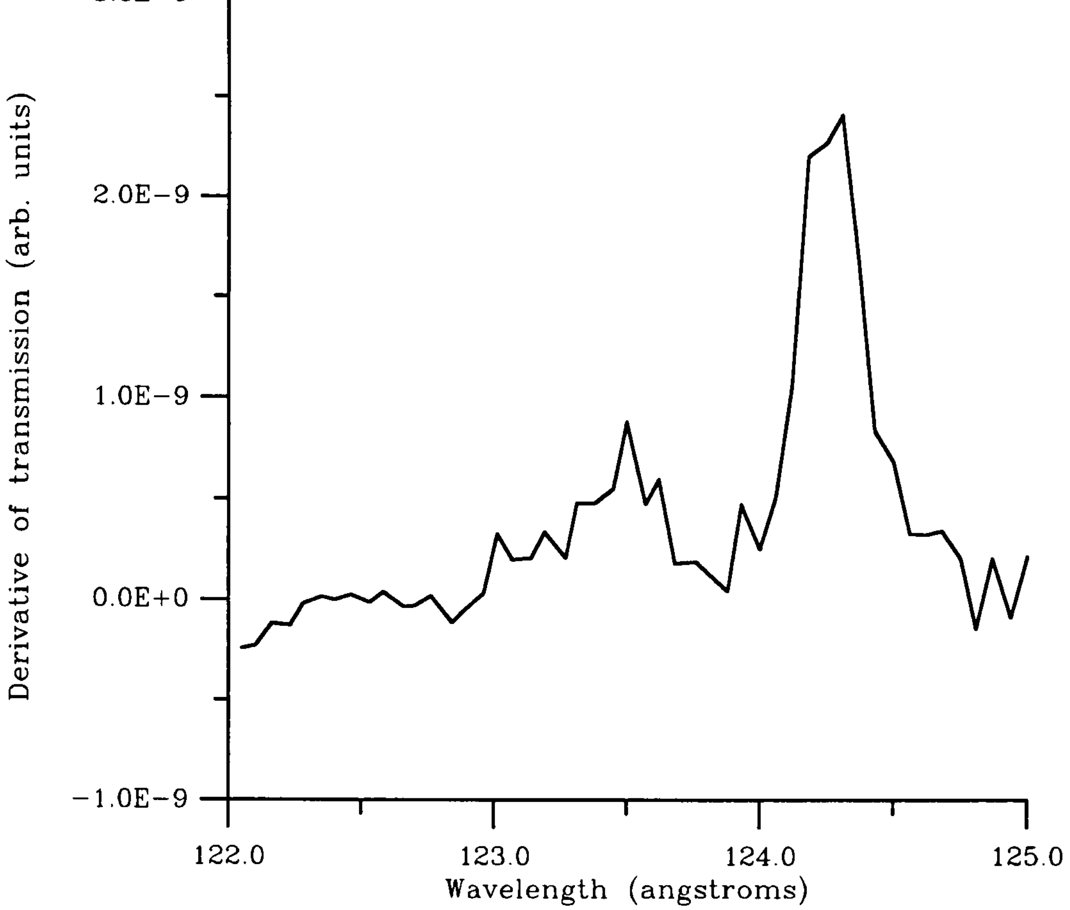

Figure 37. Silicon absorption edge recorded using electron energy loss spectroscopy (see [27]).

resolving powers, the data show good qualitative agreement with the predicted trends; the high energy grating generally resolves better than the low energy grating, and the resolving power of the high energy grating peaks around 120 angstroms.

The throughput of the monochromator has also been measured by recording the current from the photodiode above the absorption edge of Al. Knowing the quantum efficiency of the photodiode, the number of photons/sec/mA through the exit slit can be calculated. At 170 angstroms, SURF II provides 4 x 10^{11} photons/sec/mA into a 3 mrad vertical by 20 mrad horizontal region over a wavelength range of 0.7 angstroms. With the entrance and exit slits both set at 0.05 cm, the bandpass of the monochromator is about 0.7 angstroms. The current from the photodiode is 1.7 x 10^{-8} amp per milliamp of stored beam current corresponding to 6 x 10^{9} photons/sec/mA after the monochromator exit slit. Thus the throughput of the monochromator has been measured to be 1.6%. It is believed that the predicted throughput is artificially large because of an unusually large grating efficiency, calculated by SHADOW, of 88%. In practice, typical grating efficiencies are on the order of 10%. Using typical values for the grating efficiency, the predicted throughput would be on the order of 2%, thus showing the measured value to be in very good agreement with the prediction.

The new beamline is intended to replace an older monochromator and reflectometer facility used to characterize soft x-ray optics. The previous monochromator has a resolving power on the order of 100 and throughput of 2 x 10^{7} photons/sec/mA at 130 angstroms. Even with the natural line widths limiting the measured resolving power, the new beamline is a significant improvement over the previous instrument. While the measured resolving powers of the new monochromator are sufficient for the immediate intended use of the beamline, further characterization of the monochromator could be accomplished by examining the absorption spectra of rare gases such as xenon and argon. These gases exhibit structures sufficiently narrow to measure resolving powers in excess of 1000, thus allowing the predicted resolving power of 1400 at 100 angstroms to be tested.

8. SUMMARY

The design and performance of the NIST bl-7 varied line space grating monochromator has been discussed. This monochromator, using two interchangeable gratings, operates in the soft x-ray region of a synchrotron light source. A brief overview of the characteristics of synchrotron radiation has been presented. The unique design requirements of a beamline operating in the soft x-ray region and an overview of some standard monochromator designs have been discussed. After a thorough investigation of the focusing properties of the varied line space grating, the imaging properties, resolving power and throughput of the monochromator design were studied using the SHADOW ray tracing software package. Resolving powers in excess of 1000 and throughput on the order of 8×10^9 are predicted.

Initial alignment of the monochromator optical system using zero-order light has been discussed. Commissioning of the beamline has produced resolving powers as high as 730 at 124 angstroms and throughput of 6×10^9 photons/sec/mA at 170 angstroms. These results were obtained by scanning the monochromator over the absorption edges of Al, Be, C and Si thin films. Direct measurement of the instrument resolving power is limited by broad natural linewidths of the films at room temperature. Further work using gas phase absorption spectra could test the predicted upper limit of the instrument resolving power.

LIST OF REFERENCES

REFERENCES

1. D. H. Tomboulian and P. L. Hartman, Phys. Rev. **102**, 1423 (1956).
2. D. Ivanenko and I. Pomeranchuck, Phys. Rev. **65**, 343 (1944).
3. E. M. McMillan, Phys. Rev. **68**, 143 (1945).
4. L. I. Schiff, Rev. Sci. Instrum. **17**, 6 (1946).
5. J. Schwinger, Phys. Rev. **70**, 798 (1946) and **75**, 1912 (1949).
6. F. R. Elder, A. M. Gurewitsch, R. V. Langmuir, and H. C. Pollock, Phys. Rev. **71**, 829 (1947).
7. T. A. Callcott, W. L. O'Brien, J. J. Jia, Q. Y. Dong, D. L. Ederer, R. N. Watts, and D. R. Mueller, Nucl. Instrum. and Meth. A**319**, 128 (1992).
8. G. Margaritondo, Introduction to Synchrotron Radiation, Oxford University Press, New York (1988).
9. For a discussion of the use of multiple mirrors to reduce aberrations, see A. of G. Michette's, Optical Systems For Soft X-rays, section 2.4, Plenum Press, New York (1986).
10. See for example, Proceedings of the Fourth International Conference on Synchrotron Radiation Instrumentation, 15 - 19 July, 1991, Chester, United Kingdom, Rev. Sci. Instrum. **63** (1992).
11. F. C. Brown, R. Z. Bachrach, and N. Lien, Nucl. Instrum. and Meth. **152**, 73 (1978).
12. J. L. Rose, D. C. Mancini, J. T. Walnak and R.K. Cole, Nucl. Instrum. and Meth. A**291**, 192 (1990).
13. D. C. Mancini, M. Bissen, D. Rioux, R. Patel, G. Rogers, E. L. Brodsky and H. Höchst, Rev. Sci. Instrum. **63**, 1269 (1992).
14. P. de T. Fonseca, H. G. Pacheco E. d'A Samogin, and A. R. B. de Castro, Rev. Sci. Instrum. **63**, 1256 (1992).

15. C. T. Chen, F. Sette and N. V. Smith, Appl. Opt. **29**, 4536 (1990).

16. C. T. Chen, Rev. Sci. Instrum. **63**, 1229 (1992).

17. S. Aksela, A. Kivimäki, R. Nyholm, and S. Svensson, Rev. Sci. Instrum. **63**, 1252 (1992).

18. M. C. Hettrick, J. H. Underwood, P. J. Batson, and M. J. Eckart, Appl. Opt. **27**, 200 (1988).

19. M. Itou, T. Harada and T. Kita, Appl. Opt. **28**, 146 (1989).

20. T. Harada, Nucl. Instrum. and Meth. **A291**, 179 (1990).

21. W. R. McKinney, Rev.Sci. Instrum. **63**, 1410 (1992).

22. Glidcop is a copper alloy commercially available from Tucson Optical Research Company.

23. ULE quartz is fused quartz designed for use with ultraviolet radiation and is commercially available from Tucson Optical Research Company.

24. A. Ejiri, S. Yamaguchi, M. Saruwatari, M. Yokota, K. Inayoshi and G. Mutsuoka, Opt. Commun. **1**, 349 (1970).

25. F. C. Brown, R. Z. Bachrach and M. Skibowski, Phys. Rev. **B15**, 4781 (1977).

26. R. S. Crisp, J. Phys. **F10**, 511, 2313 (1980).

27. C. P. Franck, S. E. Schnatterly, F. H. Zutavern, T. Aton, T. Cafolla and R. D. Carson, Phys. Rev. **B31**, 5366 (1985).

28. C. Tarrio and S. E. Schnatterly, J. Opt. Soc. Am. **B10**, 952 (1993).

APPENDIX

APPENDIX

The convolution theorem is used to show that the convolution of two Gaussian functions, $G_1(x)$ and $G_2(x)$, is another Gaussian, $G_R(x)$, with $\sigma_R^2 = \sigma_1^2 + \sigma_2^2$. From the convolution theorem, we know that the Fourier transform of the convolution of two functions is equal to the product of the Fourier transforms of the functions:

$$FT\left\{\int_0^x G_1(x)G_2(x-\tau)d\tau\right\} = FT\{G_1(x)\}FT\{G_2(x)\} \tag{A1}$$

We know that the Fourier transform of a Gaussian is another Gaussian of the form: $e^{-k^2\sigma^2/2}$, thus the right hand side of equation (A1) is just the product of two Gaussians: $e^{-k^2(\sigma_1^2+\sigma_2^2)/2}$. Taking the inverse Fourier transform gives a Gaussian:

$$G_R(x) = \frac{1}{\sqrt{2\pi(\sigma_1^2+\sigma_2^2)}}e^{-x^2/2(\sigma_1^2+\sigma_2^2)}. \tag{A2}$$

We can now easily identify $G_R(x)$ as a Gaussian function with $\sigma_R^2 = \sigma_1^2 + \sigma_2^2$.

VITA

Michael Haass was born in Chicopee, Massachusetts on June 4, 1965. He attended elementary school in the small Florida towns of Valparaiso and Niceville and graduated from Niceville Senior High School in 1983. Two years of work were enough to convince him to return to school at Santa Fe Community College in Gainesville, Florida in the Fall of 1985. He graduated with an Associate of Arts degree in August, 1987 and transferred to The University of West Florida in Pensacola, Florida where he received a Bachelor of Science in Physics in May 1990. A Science Alliance summer fellowship brought him to The University of Tennessee in June, 1990 and he continued there to complete a Master's of Science in Physics in August, 1993.

Taking the words "go West young man" to heart, Mike is moving to Albuquerque, New Mexico in August, 1993 to seek work in the field of optics.